Sub-Decadal Volcanic Tsunamis Due To Submarine Trapdoor Faulting at Sumisu Caldera in the Izu-Bonin Arc

Osamu Sandanbata, Shingo Watada, Kenji Satake, Hiroo Kanamori, Luis Rivera, Zhongwen Zhan

HAL Id: insu-03824789
https://insu.hal.science/insu-03824789

Submitted on 21 Oct 2022

JGR Solid Earth

RESEARCH ARTICLE

Key Points:

- Large tsunamis are generated by moderate-sized volcanic earthquakes at a submarine caldera
- Tsunami and seismic data indicate that abrupt uplift of the submarine caldera by trapdoor faulting causes large tsunamis
- Continuous magma supply into the submarine caldera induces submarine trapdoor faulting on a decadal timescale

Supporting Information:

Supporting Information may be found in the online version of this article.

Correspondence to:

O. Sandanbata,
osm3@bosai.go.jp

Sub-Decadal Volcanic Tsunamis Due To Submarine Trapdoor Faulting at Sumisu Caldera in the Izu–Bonin Arc

Osamu Sandanbata[1,2] ![ORCID], Shingo Watada[1] ![ORCID], Kenji Satake[1] ![ORCID], Hiroo Kanamori[3] ![ORCID], Luis Rivera[4], and Zhongwen Zhan[3] ![ORCID]

[1]Earthquake Research Institute, The University of Tokyo, Bunkyo, Tokyo, Japan, [2]Now at National Research Institute for Earth Science and Disaster Resilience, Tsukuba, Ibaraki, Japan, [3]Seismological Laboratory, California Institute of Technology, Pasadena, CA, USA, [4]Université de Strasbourg, CNRS, ITES UMR 7063, Strasbourg, France

Abstract The main cause of tsunamis is large subduction zone earthquakes with seismic magnitudes $M_w > 7$, but submarine volcanic processes can also generate tsunamis. At the submarine Sumisu caldera in the Izu–Bonin arc, moderate-sized earthquakes with $M_w < 6$ occur almost once a decade and cause meter-scale tsunamis. The source mechanism of the volcanic earthquakes is poorly understood. Here we use tsunami and seismic data from the recent 2015 event to show that abrupt uplift of the submarine caldera, with a large brittle rupture of the ring fault system due to overpressure in its magma reservoir, caused the earthquake and tsunami. This submarine trapdoor faulting mechanism can efficiently generate tsunamis due to large vertical seafloor displacements, but it inefficiently radiates long-period seismic waves. Similar seismic radiation patterns and tsunami waveforms due to repeated earthquakes indicate that continuous magma supply into the caldera induces quasi-regular trapdoor faulting. This mechanism of tsunami generation by submarine trapdoor faulting underscores the need to monitor submarine calderas for robust assessment of tsunami hazards.

Plain Language Summary Tsunamis are mainly caused by large submarine earthquakes, but submarine volcanic processes can also trigger tsunamis. Disproportionately large tsunami waves have been generated every decade by moderate-sized volcanic earthquakes at a submarine volcano with a caldera structure, called Sumisu caldera, in the Izu–Bonin arc, south of Japan. Despite the moderate earthquake size, the maximum wave heights of the tsunamis were about a meter, and their source mechanism has been controversial. In this study, we used tsunami and seismic data from a recent earthquake to show that the submarine caldera abruptly uplifts due to brittle rupture of its intra-caldera fault system driven by overpressure of magma accumulating in its underlying magma reservoir and generates large tsunamis almost once a decade. The atypical source mechanism for tsunami generation suggests that it is important to monitor active submarine calderas for assessing tsunami hazards.

1. Introduction

Large earthquakes in subduction zones with seismic moment magnitudes $M_w > 7$ are the main causes of tsunamis, but other submarine geophysical processes, such as volcanism or landslides, can also trigger tsunamis (Kanamori, 1972; Paris, 2015; Satake, 2015; Ward, 2001). Because the latter generally do not cause significant seismic ground motion, the difficulty in forecasting tsunamis results in increased tsunami risk to coastal societies (Grilli et al., 2019; Hunt et al., 2021; Tappin et al., 1999; Walter et al., 2019). Unusual tsunamis have been reported for earthquakes generated at Sumisu caldera (also known as Smith caldera), which is a submarine volcano with an 8×10 km caldera structure in the Izu–Bonin arc (Figure 1) (Shukuno et al., 2006; Tani et al., 2008). At the caldera, volcanic earthquakes with moderate seismic magnitudes (M_w 5.4–5.7) have occurred quasi-regularly in 1984, 1996, 2006, 2015, and 2018 (Figure 1b; Table S1 in Supporting Information S1), which are known as Torishima earthquakes (Fukao et al., 2018; Kanamori et al., 1993; Satake & Kanamori, 1991). The earthquake on 2 May 2015 (M_w 5.7) caused a disproportionally large tsunami with a maximum wave height of 1 m on Hachijojima Island, located 180 km north of the caldera (Figure 1c), although no ground shaking was felt on the island. The other four earthquakes also caused relatively large tsunamis with similar waveforms at many tide gauge stations (Figures 1d–1e and Figure S1 in Supporting Information S1). The five earthquakes were seismologically similar to each other, and all had a moment tensor with a large compensated-linear-vector-dipole (CLVD) component and a dominant nearly vertical tension axis (Figure 1b), which is often called a vertical-T CLVD earthquake (Shuler, Ekström, & Nettles, 2013; Shuler, Nettles, & Ekström, 2013).

Visualization: Osamu Sandanbata
Writing – original draft: Osamu Sandanbata
Writing – review & editing: Shingo Watada, Kenji Satake, Hiroo Kanamori, Luis Rivera, Zhongwen Zhan

Since the 1984 earthquake, various models have been proposed for this atypical earthquake mechanism and tsunami generation. These include dip slip on a curved ring fault system of a caldera (Ekström, 1994), vertical opening of a shallow horizontal crack (Fukao et al., 2018), and volume change due to fluid injection at shallow depth (Kanamori et al., 1993; Satake & Kanamori, 1991). However, different interpretations can explain the moment tensors (Shuler, Ekström, & Nettles, 2013), and no consensus on the earthquake mechanism has yet been reached, because of the inaccessibility of the submarine caldera. For the 2015 earthquake, the tsunami was recorded by high-quality ocean bottom pressure (OBP) gauges of a temporary array and recently deployed tsunami observation networks to the south of Japan (Figure 1a). The obtained tsunami waveform and regional seismic data provide an opportunity to determine the mechanisms responsible for these anomalous volcanic earthquakes.

The objective of this study is to determine the source mechanism of the volcanic earthquakes at Sumisu caldera. We initially conduct a preliminary analysis using only the tsunami waveform data from the 2015 event to estimate the sea-surface disturbance due to the coseismic seafloor deformation. We then combine the tsunami and long-period seismic waveform data analyses to develop a source model that can quantitatively explain both datasets. Based on this model, we discuss the source mechanism of the earthquakes, possible causes of the efficient tsunami excitation and their sub-decadal recurrence, and implications for the submarine volcanism of Sumisu caldera.

2. Data

2.1. Tsunami Data

We use tsunami data from the 2015 earthquake recorded by 24 OBP gauges (Figure 1a) of the array off Aogashima Island, the Dense Oceanfloor Network system for Earthquakes and Tsunamis (DONET) system, the Deep Sea Floor Observatory (DSFO) off Muroto Cape, and the Deep-ocean Assessment and Reporting of Tsunamis (DART) system. We manually check the data quality (i.e., data gaps, spikes, or repeated values) near the arrival times of the tsunami signals and remove tidal trends by fitting polynomial functions. Following Sandanbata, Watada, et al. (2021), we apply a two-pass second-order low-pass Butterworth filter to the tsunami waveforms. The cut-off frequencies are 0.0125, 0.0083, 0.0083, and 0.00667 Hz for stations from the array, DONET, DSFO, and DART, respectively, depending on the maximum depth along a source–station path.

2.2. Long-Period Seismic Data

We use seismic data from the 2015 earthquake recorded by the BH channel (three components) of 36 regional stations (epicentral distance <30°) of the F-net and Global Seismograph Network (GSN). The seismic stations are listed in Table S2 in Supporting Information S1. We remove the instrument response from the observed seismograms to obtain the displacement records and apply a one-pass fourth-order band-pass Butterworth filter with corner frequencies of 0.004 and 0.0167 Hz (band-pass period = 60–250 s) using the W-phase package (Duputel et al., 2012; Hayes et al., 2009; Kanamori & Rivera, 2008).

3. Preliminary Analysis: Estimation of the Initial Sea-Surface Displacement

As a preliminary step for the source modeling of the 2015 earthquake, we estimate the initial sea-surface displacement caused by the earthquake using a tsunami waveform inversion method. To compute synthetic tsunami waveforms, we first assume 113 unit sources of sea-surface displacement at 2 km intervals in a source area of 32×32 km around Sumisu caldera (Figure S2 in Supporting Information S1). Each unit source has a cosine-tapered shape (Hossen et al., 2015):

$$\eta^k(x, y) = 0.25 \times \left[1.0 + \cos\frac{\pi\left(x - x^k\right)}{L}\right] \times \left[1.0 + \cos\frac{\pi\left(y - y^k\right)}{L}\right], \; \left(|x - x^k|, \, |y - y^k| \leq L\right) \quad (1)$$

where $\left(x^k, y^k\right)$ is the central location in kilometers of the kth unit source ($k = 1, 2, \ldots, K$; here $K = 113$) with a source size of $2L$ (i.e., 4.0 km). The rise time for each unit source is 10 s, given that the earthquake source duration is 10 s as estimated by our moment tensor analysis (Text S1 and Table S3 in Supporting Information S1).
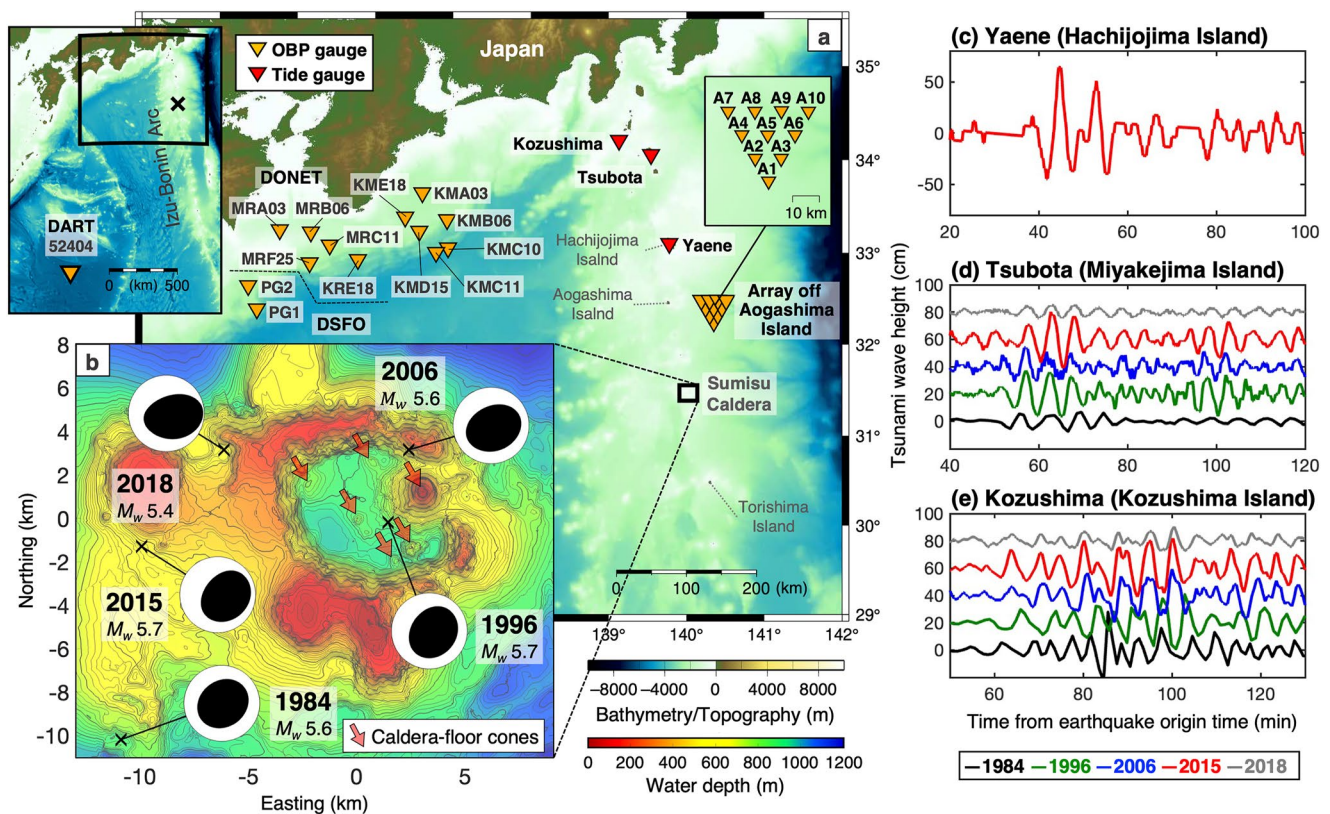
Figure 1. Anomalous tsunamis due to volcanic earthquakes at Sumisu caldera. (a) Map showing the locations of Sumisu caldera, ocean bottom pressure gauges (orange triangles), and representative tide gauges (red triangles). (b) Repeating earthquakes near Sumisu caldera reported by the Global CMT (GCMT) catalog (Ekström et al., 2012). The focal mechanisms are shown by projection of the lower focal hemisphere. Arrows point to cones on the caldera floor, some of which were identified as lava domes (Tani et al., 2008). (c) Tsunami waveform from the 2015 earthquake recorded by the tide gauge at Yaene (Hachijojima Island). (d–e) Tsunami waveforms at Tsubota (Miyakejima Island) and Kozushima (Kozushima Island) from the repeating earthquakes. Baselines for different events are shifted by multiples of 20 cm. Tsunami waveforms at other tide gauge stations are shown in Figure S1 in Supporting Information S1.

We then simulate tsunami propagation over the ocean from the assumed unit sources. To compute a tsunami waveform with relatively long-period components at the most distant station 52,404 (located ~1,400 km from the epicenter), we use a phase correction method developed for long-period tsunamis (Ho et al., 2017). In this method, we first solve the linear long-wave equations with the JAGURS code (Baba et al., 2015) and then correct the phase spectra to incorporate the effects of the dispersion, the compressibility and the density stratification of seawater, and the elasticity of the Earth. On the other hand, tsunami waveforms at the other stations at shorter distances are dominated by shorter-period waves, which makes it inadequate to use the linear long-wave equations. Hence, we use a different phase correction method that was developed for short-period tsunamis (Sandanbata, Watada, et al., 2021). In this method, we solve the linear Boussinesq equations (Peregrine, 1972; approximately including dispersion) by the JAGURS code and corrected the phase spectra to incorporate the accurate dispersion, the effects of seawater compressibility and density stratification, and the Earth's elasticity. The latter phase correction method incorporates variations in ray paths of highly dispersive short-period waves and enables us to compute short-period waveforms more accurately. In both cases, the computational time-step interval is 0.25 s. We use high-resolution bathymetric data (10 arcsec, ~300 m, grid spacing) processed from M7000 Digital Bathymetric Chart (M7022) for the area near Sumisu caldera and Aogashima Island, whereas we use JTOPO30 and GEBCO_2014 (30 arcsec grid spacing) for the other regions. When the tsunami wavelength is comparable to or shorter than the water depth, the bottom pressure change becomes smaller and smoother than that just beneath the sea surface which is equivalent to the static water pressure of the wave height. To include this pressure reduction effect, we apply a spatial low-pass filter, often referred to as the Kajiura filter (Kajiura, 1963), to the wave-height field output for every 5.0 s and obtain the OBP change at the stations (Chikasada, 2019). We also apply the low-pass Butterworth filter to the time series of the OBP change as used for the OBP data. Hereafter, the tsunami waveforms are OBP waveforms (in the [cm H$_2$O] scale).

After computing the synthetic tsunami waveforms $g_j^k(t)$ from the kth unit source to the jth station ($j = 1, 2, \ldots, J$; here $J = 24$), we solve a linear inverse problem to estimate the initial sea-surface displacement. Because the wave amplitudes of the near-field data (a few centimeters) are much larger than those of the regional-field data (a few millimeters), we normalize the observed and synthetic waveforms at the jth station by the weight w_j, following the method of Ho et al. (2017). The weight is the inverse root-mean-square (RMS) value of the observed waveform at each station:

$$\frac{1}{w_j} = \sqrt{\frac{\sum_{l=0}^{\gamma_j} \{d_j(t_l)\}^2}{\gamma_j}}, \tag{2}$$

where $d_j(t_l)$ is the tsunami waveform data for the jth station and γ_j is the number of data points used for the analysis. Using the normalized observed and synthetic waveform data, we solve the following observation equation with the damped least-squares method (pp. 695–699 in Aki & Richards, 1980):

$$\begin{bmatrix} \overline{d} \\ 0 \end{bmatrix} = \begin{bmatrix} \overline{g} \\ \alpha I \end{bmatrix} m, \tag{3}$$

where $\overline{d} = \begin{bmatrix} w_1 d_1(t) & \cdots & w_J d_J(t) \end{bmatrix}^T$ and $\overline{g} = \begin{bmatrix} w_1 g_1^1(t) & \cdots & w_1 g_1^K(t) \\ \vdots & \ddots & \vdots \\ w_J g_J^1(t) & \cdots & w_J g_J^K(t) \end{bmatrix}$ are the column vector of the observed

waveform data $d_j(t)$ and the matrix of the synthetic waveform data $g_j^k(t)$ weighted by w_j at the jth station (Equation 2), respectively, and $m = \begin{bmatrix} m^1 & \cdots & m^K \end{bmatrix}^T$ is an unknown column vector of the amplitude factors to be multiplied by the kth unit source, I is the identity matrix, and α is the damping parameter used to obtain a smooth model. We assume $\alpha = 2.0$ to achieve an appropriate trade-off between the waveform fit and the smoothness of the solution (Figure S3 in Supporting Information S1).

Thus, we obtain an initial sea-surface displacement model, composed of a sea-surface uplift of about 1 m over the caldera floor, with its uplift peak shifted northeastward relative to the caldera center, and smaller subsidence outside of the caldera rim mainly on the northeastern side (Figure 2a). This model reproduces the tsunami waveform data (Figure S4 in Supporting Information S1). To examine the robustness of the exterior subsidence, we estimate the initial sea-surface uplift model, without subsidence, by imposing a non-negative condition ($m \geq 0$) when solving Equation 3. The obtained uplift model, containing only a larger northeastern uplift, cannot reproduce the tsunami first motions with initial downswing signals of the relatively near-field stations in the northeastern direction (A01–A10; Figure 2b). This result suggests that, during the earthquake, the exterior of the caldera subsided at least on its northeastern side. Note that a previous study (Fukao et al., 2018) assumed a symmetrical caldera floor uplift model surrounded by peripheral subsidence to explain the tsunami waveforms at the array off Aogashima Island, but Sandanbata, Watada, et al. (2021) demonstrated that the model of Fukao et al. (2018) does not explain the tsunami arrival times at the stations of DONET, DSFO and DART. Our tsunami waveform inversion using all the OBP data with wider azimuthal coverage suggests that the uplift and the subsidence were localized on the northeastern side of the caldera.

4. Source Modeling of the 2015 Earthquake: Methodology

4.1. Hypothetical Earthquake Source System

We next explore the source model of the 2015 earthquake by combining analyses of the tsunami and long-period seismic data. From the deformation pattern determined in the preliminary analysis (Section 3), we assume an earthquake source system composed of dip slip of an elliptical fault system and vertical deformation of a shallow horizontal crack beneath Sumisu caldera (Figure 3a). This assumption of the fault-crack composite system is inspired by previous caldera modeling studies that discussed interactive systems beneath calderas between a circular or elliptical fault, called *ring fault*, and a sill-like magma reservoir (e.g., Bathke et al., 2015; Galetto et al., 2019; Liu et al., 2019; Yun, 2007; Zheng et al., 2022). Most calderas are known to have pre-existing ring
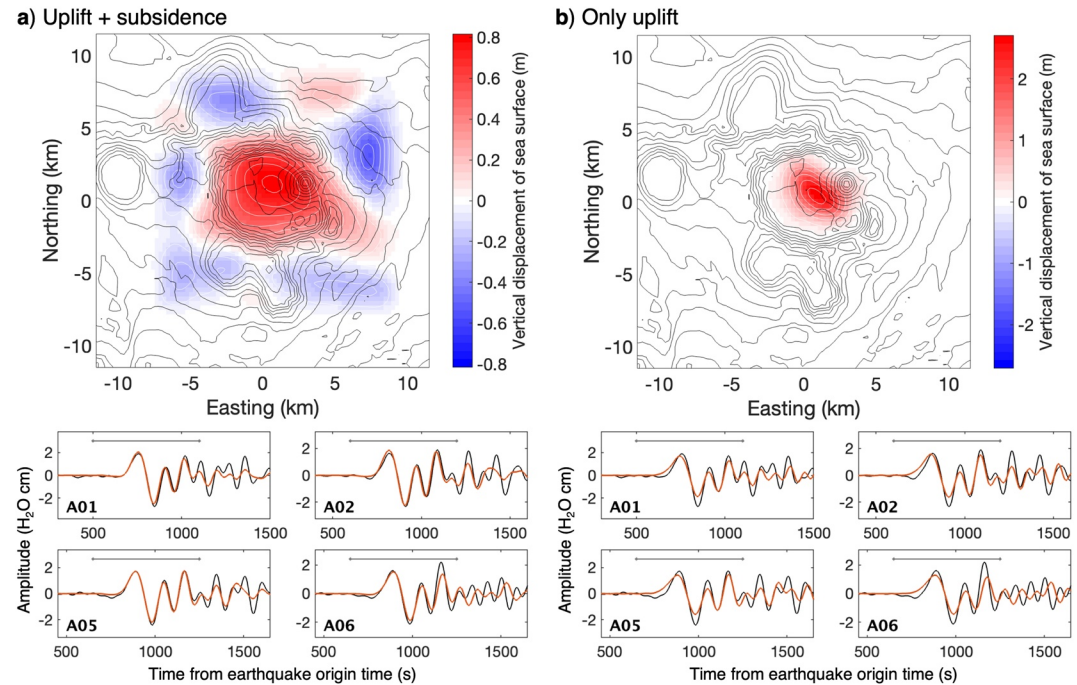
Figure 2. Preliminary initial sea-surface displacement models. Models with (a) both uplift and subsidence and (b) only uplift. (Top panel) Red and blue colors represent uplift and subsidence, respectively. Bathymetric contours at 100 m intervals. (Bottom panels) Comparison of the observed (black) and synthetic (red) tsunami waveforms at representative ocean bottom pressure gauges. The gray line represents the time interval used for the inversion.

fault systems formed during caldera collapse in the past (e.g., Cole et al., 2005; Roche et al., 2000), where faulting events called *ring-faulting* sometimes take place in response to pressure change in an underlying magma reservoir (e.g., Contreras-Arratia & Neuberg, 2019; Ekström, 1994; Sandanbata, Kanamori, et al., 2021; Shuler, Ekström, & Nettles, 2013). For example, at the subaerial caldera of Sierra Negra in the Galapagos Islands, seismic events characterized by vertical-T CLVD moment tensors occurred in such a sub-caldera interactive system, and caused large asymmetric uplifts of the caldera floor (e.g., Amelung et al., 2000; Chadwick et al., 2006; Jónsson, 2009) like what was estimated for the 2015 earthquake at Sumisu caldera in Section 3. Some previous studies (e.g., Yun, 2007; Zheng et al., 2022) explained geodetic data at Sierra Negra caldera by proposing source models that combine ring-faulting and deformation of its underlying horizontal crack; this inferred mechanism is especially referred to as *trapdoor faulting*. Given such successful examples of caldera modeling, the fault-crack composite system can be a good candidate for the earthquake source at Sumisu caldera. Caldera-floor cones, some of which were identified as young lava domes (Tani et al., 2008), are located along a line forming an elliptical shape on the floor of Sumisu caldera (Figure 1b); this also indicates that a ring fault system is connected to a shallow reservoir filled with magma (Cole et al., 2005).

4.2. Tsunami Waveform Inversion for Fault-Crack Composite Source Models

We again use a tsunami waveform inversion method with the OBP data but this time to directly determine motions of the fault-crack composite system (i.e., dip-slip dislocations of the ring fault and tensile dislocations of the horizontal crack). The inversion procedure is as follows.

4.2.1. Source Structure

To model the fault-crack composite system beneath Sumisu caldera, we assume reverse slip for an inward-dipping ring fault and vertical deformation (opening or closing) for a horizontal crack (Figure 3a). We consider reverse slip of the inward-dipping ring fault, because vertical-T CLVD earthquakes accompanying a caldera floor uplift are expected for the combination of the slip and dip directions of the ring-faulting (see Figure 9 in Shuler, Ekström, & Nettles, 2013, or Figure 1 in Sandanbata, Kanamori, et al., 2021). The ring fault is elliptical with its center at (140.0454°E, 31.4816°N) and its major axis oriented N70°E, and its horizontal size is 3.0 × 2.7 km
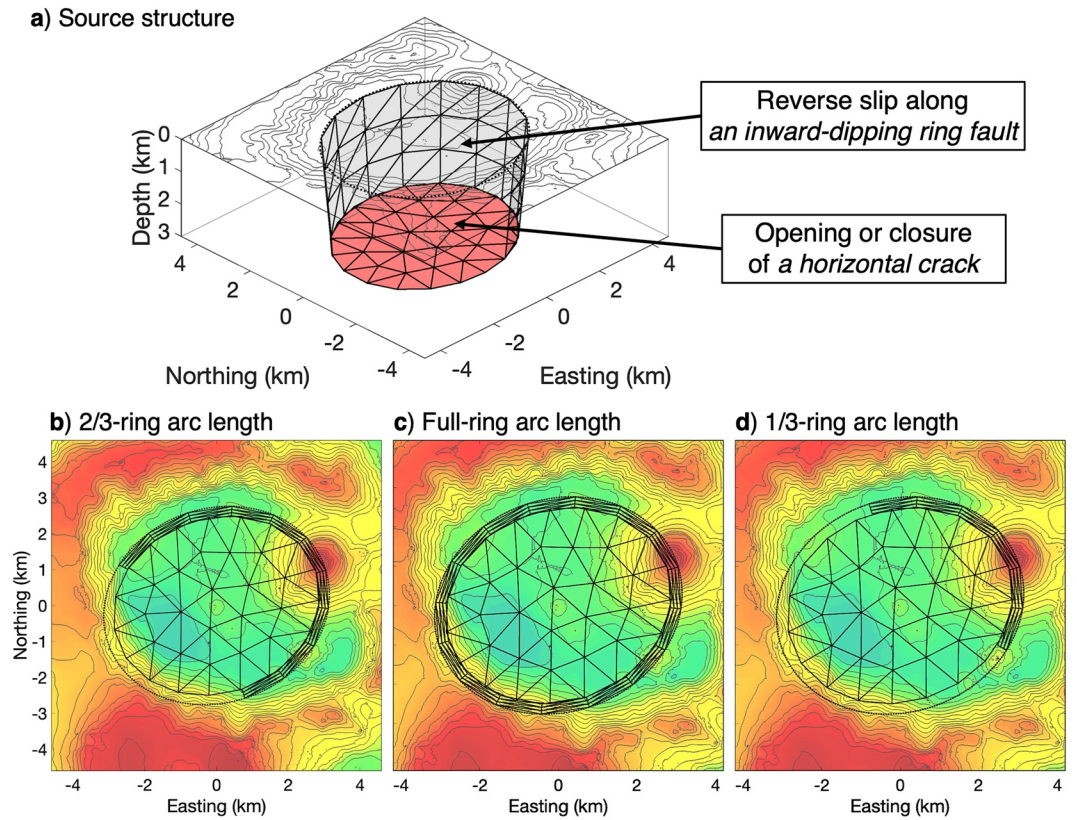
Figure 3. Fault-crack composite system assumed for the source modeling. (a) Example of the source structure assumed in this study. (b–d) Three cases of the ring-fault arc length assumed in the source modeling: (b) 2/3 ring, (c) full ring, and (d) 1/3 ring arc lengths.

on the seafloor. The ring fault may not be a full ring; the arc length is varied as 1/3, 2/3 and 1 (full ring), but the midpoint is fixed to the northeastern corner of the caldera (Figures 3b–3d). The ring fault extends with a uniform inward dip angle from the seafloor to the edge of the elliptical horizontal crack. We try tens of source structures with three variable geometric parameters: (a) the depth of the horizontal crack (3 or 6 km); (b) the dip angle of the ring fault (70–90°); and (c) the arc length of the ring fault (1/3, 2/3, or full ring).

We discretize each source structure into triangular source elements. The ring fault is divided into triangular elements with an arc angle of 22.5° along the circumference and 1 km along the depth, and a trapezoid composed of two neighboring triangular elements with the same dip and strike angles is regarded as a sub-fault. The horizontal crack is discretized by triangular elements using the DistMesh code (Persson & Strang, 2004), and each element is regarded as a sub-crack. Assuming the geometry of sub-faults and sub-cracks, we will determine dislocation amounts of reverse slip at each sub-fault and opening (or closing) at each sub-crack, which are denoted by $\boldsymbol{s} = \begin{bmatrix} s_1 & \cdots & s_{N_s} \end{bmatrix}^T$ and $\boldsymbol{\delta} = \begin{bmatrix} \delta_1 & \cdots & \delta_{N_\delta} \end{bmatrix}^T$, respectively. Since the dislocations of the ring fault and the horizontal crack should be consistent at their contacts, we impose a kinematic condition that links the vertical component of the sub-fault slip at the ring fault bottom to the sub-crack opening/closing at the crack edge adjacent to the sub-fault. The kinematic condition can be written as:

$$s_p \sin \Delta_p = \delta_q, \tag{4}$$

where Δ_p is the dip angle of the pth sub-fault at bottom to which the qth sub-crack is adjacent.

4.2.2. Computation of the Tsunami Green's Functions

We then compute synthetic tsunami waveforms, or Green's functions G_{ij}, relating the dislocation (i.e., reverse slip of the sub-fault and vertical opening of the sub-crack) of the ith source element ($i = 1, 2, \ldots, I$; I depends on the source structures) to the tsunami waveform at the jth station. For this purpose, we reuse the synthetic tsunami

waveforms g_j^k from unit sources of sea-surface displacement η^k, which were computed in Section 3. By reusing g_j^k, we do not have to simulate tsunami propagation over the ocean as done in Section 3, which significantly reduces the computational cost and helps us to efficiently assess the inversions for tens of source structures, each of which consists of $I > 50$ source elements. The computation of G_{ij} is performed with the following three steps.

First, we calculate the vertical seafloor displacements from 1 m reverse slips of sub-faults and 1 m opening of sub-cracks with the triangular dislocation (TD) method (Nikkhoo & Walter, 2015) assuming a Poisson's ratio of 0.25 and a flat seafloor, and we convert the seafloor displacements into the vertical *sea-surface* displacements by applying the Kajiura filter (Kajiura, 1963) assuming a water depth of 800 m; this filtering process is required because the resultant vertical sea-surface displacement becomes smaller and smoother than that at the seafloor when the horizontal scale of the seafloor displacement is comparable to or smaller than the water depth (e.g., Saito & Furumura, 2009). We thus denote the vertical sea-surface displacement from the ith source element $h_i(x, y)$.

Second, the computed sea-surface displacement $h_i(x, y)$ is approximated by a linear combination of the unit sources of sea-surface displacement $\eta^k(x, y)$ (Equation 1; Figure S2 in Supporting Information S1):

$$h_i(x, y) \approx \sum_{k=1}^{K} m_i^k \eta^k(x, y),\tag{5}$$

where the amplitude factors m_i^k are obtained by a least-squares method.

Third, we obtain Green's functions relating the ith source element to the jth station by superimposing the synthetic tsunami waveforms from the kth unit sources $g_j^k(t)$ multiplied by the amplitude factors m_i^k, as follows:

$$G_{ij}(t) = \sum_{k=1}^{K} m_i^k g_j^k(t).\tag{6}$$

4.2.3. Inverse Problem

Finally, we solve the observation equation with the kinematic condition (Equation 4) by the damped least-squares method:

$$\begin{bmatrix} \bar{d} \\ 0 \\ 0 \end{bmatrix} = \begin{bmatrix} \bar{G} \\ K \\ \beta I \end{bmatrix} \begin{bmatrix} s \\ \delta \end{bmatrix},\tag{7}$$

where $\bar{d}$ is the column vector of the observed tsunami waveforms d_j normalized by w_j at the jth station (Equation 2), and $\bar{G} = \begin{bmatrix} w_1 G_{11}(t) & \cdots & w_1 G_{I1}(t) \\ \vdots & \ddots & \vdots \\ w_J G_{1J} & \cdots & w_J G_{IJ}(t) \end{bmatrix}$ is the matrix of the Green's functions G_{ij} normalized by w_j. s is an unknown column vector of reverse slip amounts for sub-faults of the ring fault, for which we impose the non-zero condition ($s \geq 0$), and δ is an unknown column vector of opening amounts for sub-cracks of the horizontal crack, for which we allow either positive (opening) or negative (closing) values. The linear equation of $K \begin{bmatrix} s \\ \delta \end{bmatrix} = 0$ represents the kinematic condition of Equation 4. β is the damping parameter for smoothing, which we set at 0.3, by balancing the waveform fit and the smoothness of the motion (Figure S5 in Supporting Information S1). The inversion time windows include several wave crests and troughs. Thus, we determine motions of the fault-crack composite system and obtain a source model based on the tsunami data.

To evaluate the model performance, we calculate the normalized root-mean-square (NRMS) misfit of the tsunami waveforms, which we term the tsunami waveform misfit:

$$\rho^t = \sqrt{\sum_j \|c_j^t - d_j^t\|^2 / \sum_j \|c_j^t\|^2},\tag{8}$$

where c_j^t and d_j^t are the column vectors of the synthetic tsunami waveforms from the model and the observed waveforms in inversion time window at the jth station, respectively. $\| \ \|$ denotes the L2 norm.

4.3. Computation of the Long-Period Seismic Waveforms

For validation of the fault-crack composite source model inverted from the tsunami data, we compute long-period seismic waveforms for the model and compare them with the long-period seismic data. Because the wavelength of seismic data we use is much longer than the size of the caldera, the seismic source can be modeled by a point-source moment tensor. The total moment tensor $\boldsymbol{M}$ of the source model is calculated as:

$$\boldsymbol{M} = \boldsymbol{M}_{RF} + \boldsymbol{M}_{HC} = \sum \boldsymbol{m}_{RF}^p + \sum \boldsymbol{m}_{HC}^q, \tag{9}$$

where $\boldsymbol{M}_{RF}$ and $\boldsymbol{M}_{HC}$ are the moment tensors of the ring fault and horizontal crack, respectively, and $\boldsymbol{m}_{RF}^p$ and $\boldsymbol{m}_{HC}^q$ are the moment tensors of the pth sub-fault slip and the qth sub-crack opening or closure, respectively (Figure S6a in Supporting Information S1). The coordinate system is (r, θ, ϕ) for [up, south, east]. $\boldsymbol{m}_{RF}^p$ is computed from the reverse slip amount and strike, dip, and rake (90°) angles of the pth sub-fault (Box 4.4 in Aki & Richards, 1980). The seismic moment is computed as $\mu s_p A_p$, where s_p and A_p are the reverse slip amount and area of the pth sub-fault, and μ is the rigidity, or Lamé's constant. $\boldsymbol{m}_{HC}^q$ is calculated as:

$$\boldsymbol{m}_{HC}^q = \begin{bmatrix} M_{rr} & M_{\theta r} & M_{\phi r} \\ M_{r\theta} & M_{\theta\theta} & M_{\phi\theta} \\ M_{r\phi} & M_{\theta\phi} & M_{\phi\phi} \end{bmatrix} = \delta_q \times A_q \times \begin{bmatrix} \lambda + 2\mu & 0 & 0 \\ 0 & \lambda & 0 \\ 0 & 0 & \lambda \end{bmatrix}, \tag{10}$$

where δ_q and A_q are the opening amount and area of the qth sub-crack, respectively (Kawakatsu & Yamamoto, 2015). Lamé's constants λ and μ are assumed to be 29.90 and 31.85 GPa, respectively, based on the P- and S-wave velocities ($V_p = 6.0$ km/s and $V_s = 3.5$ km/s) and the density ($\rho_0 = 2.6 \times 10^3$ kg/m³) in the shallowest layer of the Earth model (Figure S6b in Supporting Information S1). The scalar seismic moment of the moment tensor is $M_0 = \sqrt{\Sigma_{ij} M_{ij} M_{ij}/2}$ (pp. 166–167 in Dahlen & Tromp, 1998; Silver & Jordan, 1982), and the moment magnitude is $M_w = \frac{2}{3}\left(\log_{10} M_0 - 9.10\right)$, with M_0 in the [N m] scale (Hanks & Kanamori, 1979; Kanamori, 1977).

By assuming the moment tensor (Equation 9), we compute the long-period (60–250 s) seismic waveforms with the W-phase package (Duputel et al., 2012; Hayes et al., 2009; Kanamori & Rivera, 2008). We compute Green's functions of the seismic waveforms for the one-dimensional crustal velocity model for Japan (Figure S6b in Supporting Information S1) using the wavenumber integration method (Herrmann, 2013). We fix the centroid location at a depth of 1.5 km below the seafloor in the center of Sumisu caldera (140.053°E, 31.485°N). The half duration of the source time function and the centroid time shift relative to the origin time reported by the Global CMT (GCMT) catalog (Ekström et al., 2012; Table S1 in Supporting Information S1) are assumed to be 5 s, based on our moment tensor analysis (Table S3 in Supporting Information S1). We apply the same filter as for the seismic data (see Section 2.2) to the synthetic waveforms.

To evaluate the model performance, we calculate the NRMS misfit of the long-period seismic waveforms, which we term the seismic waveform misfit:

$$\rho^s = \sqrt{\sum_j \|c_j^s - d_j^s\|^2 / \sum_j \|c_j^s\|^2}, \tag{11}$$

where c_j^s and d_j^s are the column vectors of the synthetic and observed seismic records at the jth channels, respectively. We set the time window to include the P, S, and surface waves.

5. Source Modeling of the 2015 Earthquake: Results

By the tsunami waveform inversion, we obtain tens of fault-crack composite source models for the 2015 earthquake with different combinations of the three geometric source parameters (i.e., the depth of the horizontal crack, the dip angle and arc length of the ring fault). As an example, Figure 4a shows the result when the horizontal
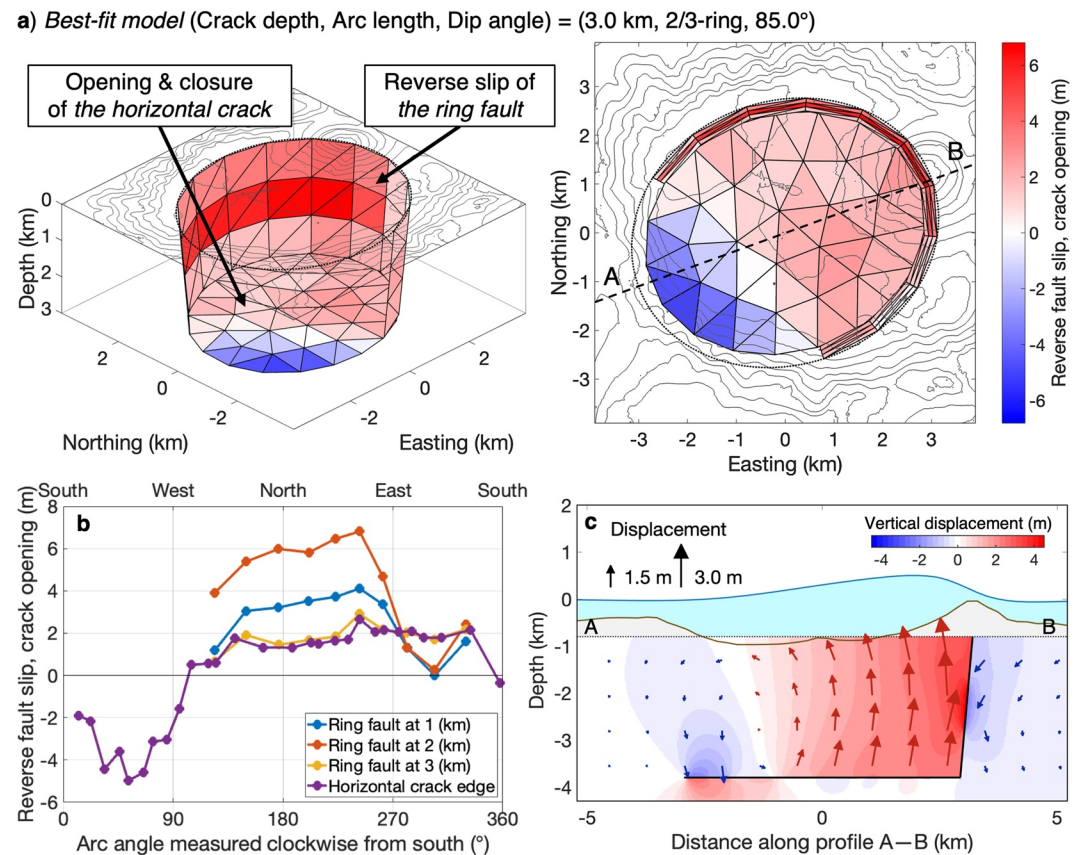
Figure 4. Best-fit source model for the 2015 earthquake. (a) Motions (dislocations) of the fault-crack composite system viewed from the southwest (left panel) and above (right panel). The horizontal crack is at a depth of 3 km, and the ring fault along two-thirds of the arc of the caldera rim has a uniform dip angle of 85°. The red color on the ring fault represents reverse slip. Red and blue colors on the horizontal crack represent vertical opening and closure, respectively. (b) Amounts of reverse slip at sub-faults of the ring fault and opening or closing of sub-cracks on the horizontal crack edge. The arc angle shown in the horizontal axis is measured clockwise from south. Circles in b are plotted at arc angles of centroids of the sub-faults and sub-cracks. Note that the ring fault displacement at the bottom (3 km) is in approximate agreement with that of the adjacent crack, because of the kinematic condition (Equation 4). (c) Displacement of the caldera computed with the model along the (a–b) profile shown in a (right panel). The red and blue colors indicate upward and downward displacements, respectively. We assume that the bathymetry is flat for the computation. Note that the seafloor and sea-surface displacements are exaggerated.

crack is at a 3 km depth and the ring fault has a dip angle of 85.0° and a 2/3-ring arc length. This model shows that the ring fault has nonzero slips at all depths that are consistent with the horizontal crack motions at the bottom (Figure 4b). The nonzero slips at all the depths are obtained for most models with the horizontal crack at a depth of 3 km. By contrast, if we assume that the horizontal crack is at a depth of 6 km, the ring fault has a zone with zero slip in the middle depth of the ring fault (Figure S7 in Supporting Information S1), which we consider unrealistic for the fault system. Hence, we suggest that the horizontal crack is at a shallower depth and hereafter show models with a horizontal crack at the depth of 3 km.

Figure 5 shows the tsunami NRMS misfit for the models with the crack at 3 km depth. The misfit varies only slightly as a function of the dip angle and the arc length of the ring fault. Figure 6 shows that the source model with a 2/3-ring arc length (shown in Figure 4a) reproduces the observed tsunami data well. Similarly, models with a full or 1/3-ring arc length yield good waveform fits (Figures S8 and S9 in Supporting Information S1). These indicate that the tsunami waveform data provide little constraint on the ring-fault parameters. However, we emphasize that, irrespective of the assumed ring-fault arc length (2/3, full, or 1/3-ring), the obtained source models are expected to similarly cause larger sea-surface uplifts over the northeastern part of the caldera but much smaller over the southwestern part (see Figure 6a, Figures S8b, and S9b in Supporting Information S1). This implies that the ring-faulting occurred mainly around the northeastern side but was minor (if any) on the southwestern side.
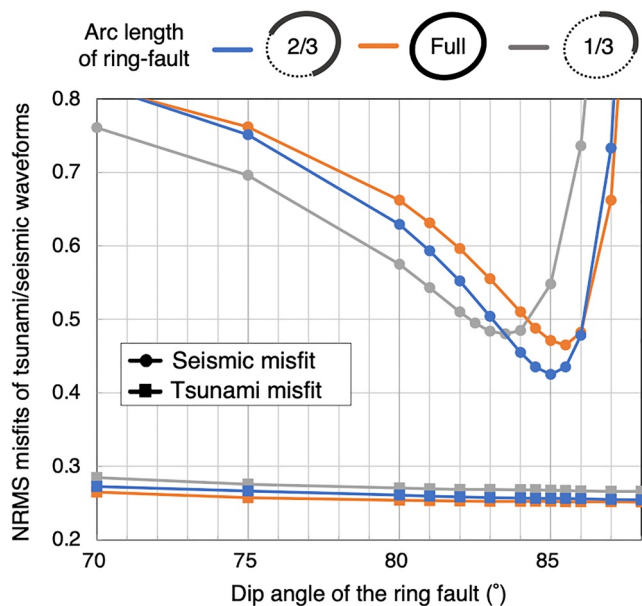
Figure 5. Comparison of the tsunami and seismic waveform misfits (Equations 8 and 11, respectively) for source models with different ring-fault dip angles and arc lengths. All the models shown here have the horizontal crack at a depth of 3 km.

To further constrain the model, we use the long-period seismic data. In contrast to the tsunami data, the seismic data are useful to constrain the ring-fault parameters. In Figure 5, we plot the seismic NRMS misfit as a function of the dip angle and the arc length of the ring fault. First, the seismic waveform misfit strongly depends on the ring-fault dip angle. Figure 7 compares fault-crack motions, moment tensors, and synthetic seismograms of three models with different dip angles (but similarly with a 2/3-ring arc length), showing that the amplitudes of seismic waveforms are significantly different despite similar slip amounts and M_w determined by the tsunami waveform inversion. This is because the ring-faulting at such a shallow depth becomes less efficient in radiating long-period seismic waves as the dip angle becomes closer to the vertical (Sandanbata, Kanamori, et al., 2021). From the seismic NRMS misfits (Figure 5), we determine optimal dip angles to be 85.0°, 85.5°, and 83.5 for 2/3, full, and 1/3-ring arc lengths, respectively. Note that if we assume a smaller rigidity for the shallow source depth, the optimal dip angles become smaller (see Text S2 in Supporting Information S1).

Among the three models with the optimal dip angles, the 2/3-ring arc-length model yields the smallest seismic NRMS misfit of 0.425 (Figure 5; 0.465 and 0.480, for the full and 1/3-ring arc lengths, respectively); this model is shown in Figure 4a. Figure 8 shows the moment tensors and synthetic seismograms for the 2/3-ring arc-length model, which overall explain the observed seismic waveforms. For comparison, we show in Figures S10 and S11 in Supporting Information S1 the cases for the full and 1/3-ring arc-length models with the optimal dip angles, respectively. The preference of the 2/3-ring arc-length model over the other two models can be seen in the better phase fits of the horizontal components at some stations (e.g., BHE channel of KZS, YMZ, and TYS, and BHN channel of AMM in Figure 8d, Figures S10d, and S11d in Supporting Information S1). As shown in Sandanbata, Kanamori, et al. (2021), the seismic radiation pattern of the ring-faulting is sensitive to the ring-fault arc length, and the side on which the ring fault is placed, because of the geometrical cancellation of double-couple components of the moment tensor (see Figure 2 of Sandanbata, Kanamori, et al., 2021). This property causes differences in seismic waveforms of the three arc-length models, which helps us to select the 2/3-ring arc-length model as the most preferable model.

In summary, based on the tsunami and seismic analyses above, we consider the model shown in Figure 4a as our best-fit source model for the 2015 earthquake. This model has a horizontal crack at a depth of 3 km and a ring fault with an inward dip angle of 85° along a 2/3-ring arc length, on both of which large dislocations are determined. The ring fault has a maximum reverse slip of 6.8 m on its northeastern side. The vertical opening of the horizontal crack is a maximum of 2.7 m on its eastern side, whereas its closure is 5.0 m on its southwestern side. The net volume increase of the horizontal crack calculated with the model is 1.26×10^7 m³. Figure 4c shows the subsurface displacements due to the combination of the ring-faulting and the crack deformation, calculated by the TD method, which represents the asymmetric motion of the caldera block. The maximum upward displacement is about 4 m on the inner side of the northeastern ring fault, while the maximum downward displacement is about 2 m on the southwestern upper wall of the horizontal crack.

The vertical sea-surface displacement caused by the best-fit source model (Figure 6a) presents uplift twice as large as and more localized than our preliminary analysis estimated (Figure 2a), but explains equally well the tsunami waveform data at all the OBP gauges (Figure 6b). Note that in the preliminary analysis, the main uplift was estimated in a relatively broader area (Figure 2a) because of no constraint from the source structure, possibly leading to the underestimation of the amplitude.

Figure 9 compares the contributions of the ring fault and the horizontal crack to tsunamis at representative stations. Tsunami waveforms from the two parts are more different at shorter distances (see A01–A04), indicating the importance of near-field tsunami observation to distinguish the two sources. We note that if we perform the tsunami waveform inversion by assuming only either the ring fault or the horizontal crack, the waveform fit clearly deteriorates (Figures S12 and S13 in Supporting Information S1), demonstrating that the fault-crack composite source model is an appropriate model for the earthquake.
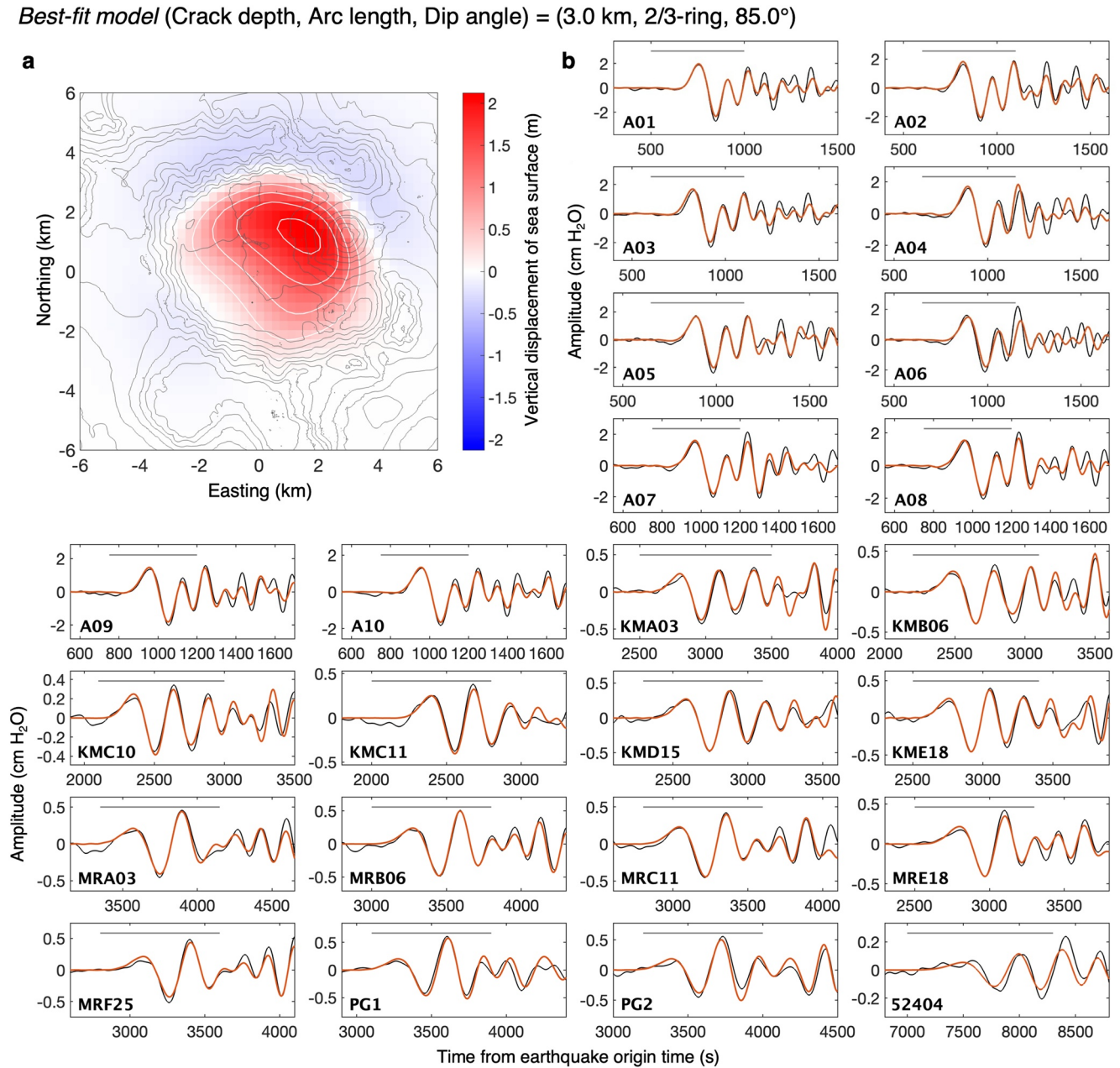
Figure 6. Tsunami waveforms from the best-fit source model (Figure 4a). (a) Vertical displacement of sea surface caused by the model. Red and blue colors represent uplift and subsidence, respectively, with white contour lines plotted every 0.5 m. Note that the color scale in this figure is different from that in Figure 2a. (b) Comparison of the observed (black) and synthetic (red) tsunami waveforms from the model at the ocean bottom pressure gauges. The gray line represents the time interval used for the inversion.

The moment tensor of the best-fit source model (Figure 8a) with a large isotropic component consists of the ring fault (Figure 8b) and the horizontal crack (Figure 8c) components. This model explains well the long-period seismic data at most stations, as shown in Figure 8d. Although slight waveform discrepancies are seen in several records (e.g., BHE channel of KZS, YMZ, and TYS, and BHN channel of AMM), they can be substantially reduced by performing the source modeling with slight modifications of dip angles in parts of the ring fault (see Text S3, Figures S14 and S15 in Supporting Information S1).

To consider contributions to long-period seismic waves from each of source parts, we show in Figure 10 long-period seismograms computed for the three partial moment tensors from our best-fit source model: (a) the ring fault only (M_{RF}: M_w 6.11); (b) the horizontal crack only (M_{HC}: M_w 5.91); and (c) the ring fault only, but
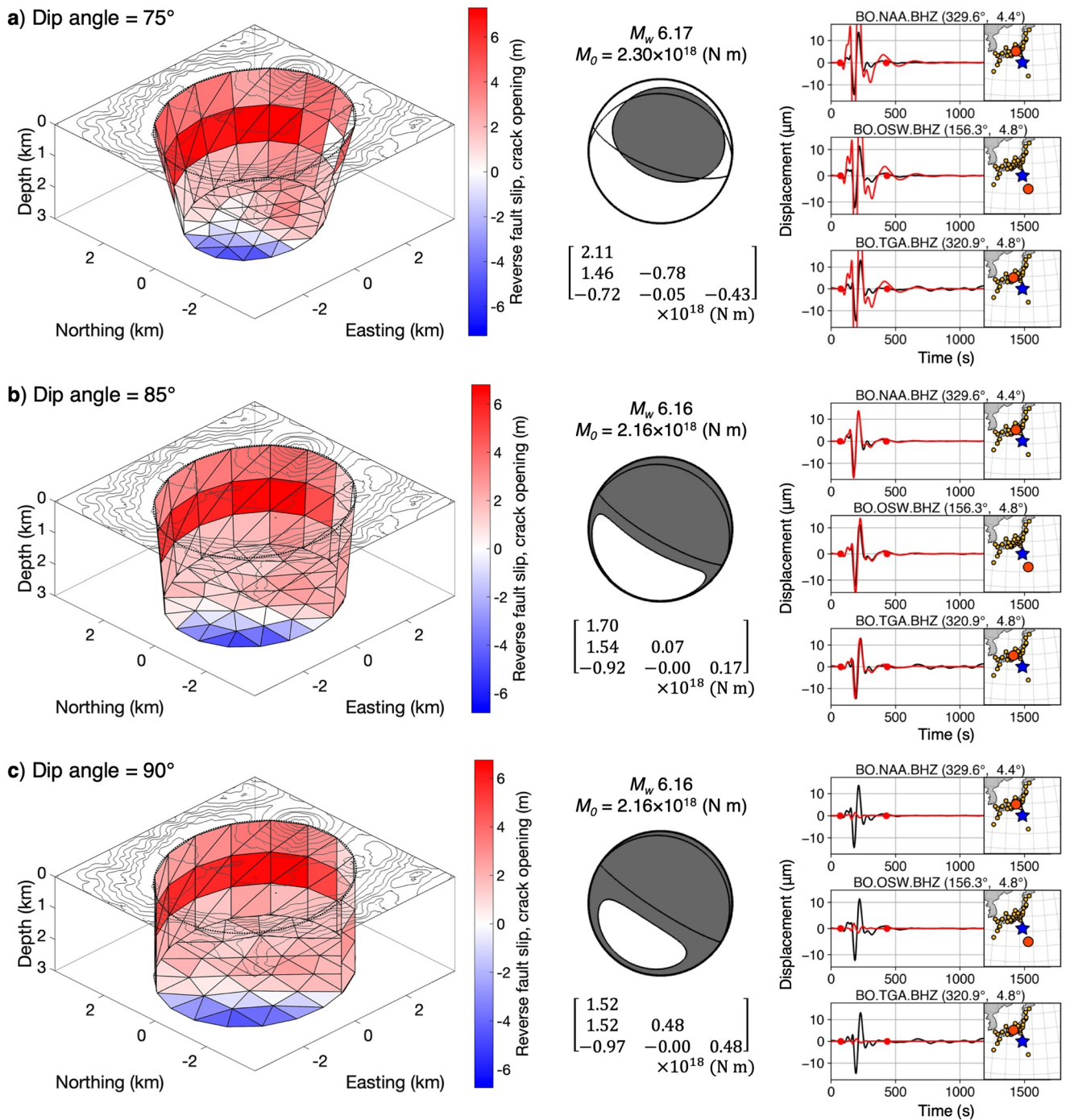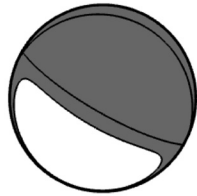
Figure 7. Long-period seismic data analyses from source models with the ring-fault dip angles of (a) 75°, (b) 85°, and (c) 90°. (Left) Motions of the fault-crack composite system inverted from the tsunami data. (Middle) Moment tensors of the model. The focal mechanisms are shown as projections of the lower focal hemisphere, and the orientation of the best double-couple solution is shown as thin lines. (Right) Comparison of the observed (black) and synthetic (red) seismograms (period = 60–250 s) at representative stations. In each inset figure, a large red circle and blue star represent the station and earthquake centroid, respectively. The network name, station name, record component, station azimuth, and epicentral distance are given on the top of each panel. Note that the amplitudes of the synthetic waveforms decrease as the ring-fault dip angle increases.

without $M_{r\theta}$ and $M_{r\phi}$ (i.e., M_{rr}, $M_{\theta\theta}$, $M_{\phi\phi}$, and $M_{\theta\phi}$ of $\boldsymbol{M_{RF}}$: M_w 5.71). The seismic magnitude of $\boldsymbol{M_{HC}}$ is comparable to that of $\boldsymbol{M_{RF}}$, but the seismic amplitudes from $\boldsymbol{M_{HC}}$ are much smaller than those from $\boldsymbol{M_{RF}}$ (compare Figures 10a and 10b). Additionally, synthetic seismograms from $\boldsymbol{M_{RF}}$ change little even after excluding the two moment tensor elements ($M_{r\theta}$ and $M_{r\phi}$; compare Figures 10a and 10c). These highlight the very small long-period

Figure 8. Long-period seismic data analyses from the best-fit source model (Figure 4a). (a) Moment tensors of the model. (b–c) Partial moment tensors of (b) the ring fault and (c) the horizontal crack. The focal mechanisms are shown as projections of the lower focal hemisphere, and the orientation of the best double-couple solution is shown as thin lines. (d) Comparison of the observed (black) and synthetic (red) seismograms (period = 60–250 s), computed with the moment tensor shown in (a) at representative stations. The data interval used to calculate the waveform misfit is delimited by the red dots. See the caption for the right panel of Figure 7.

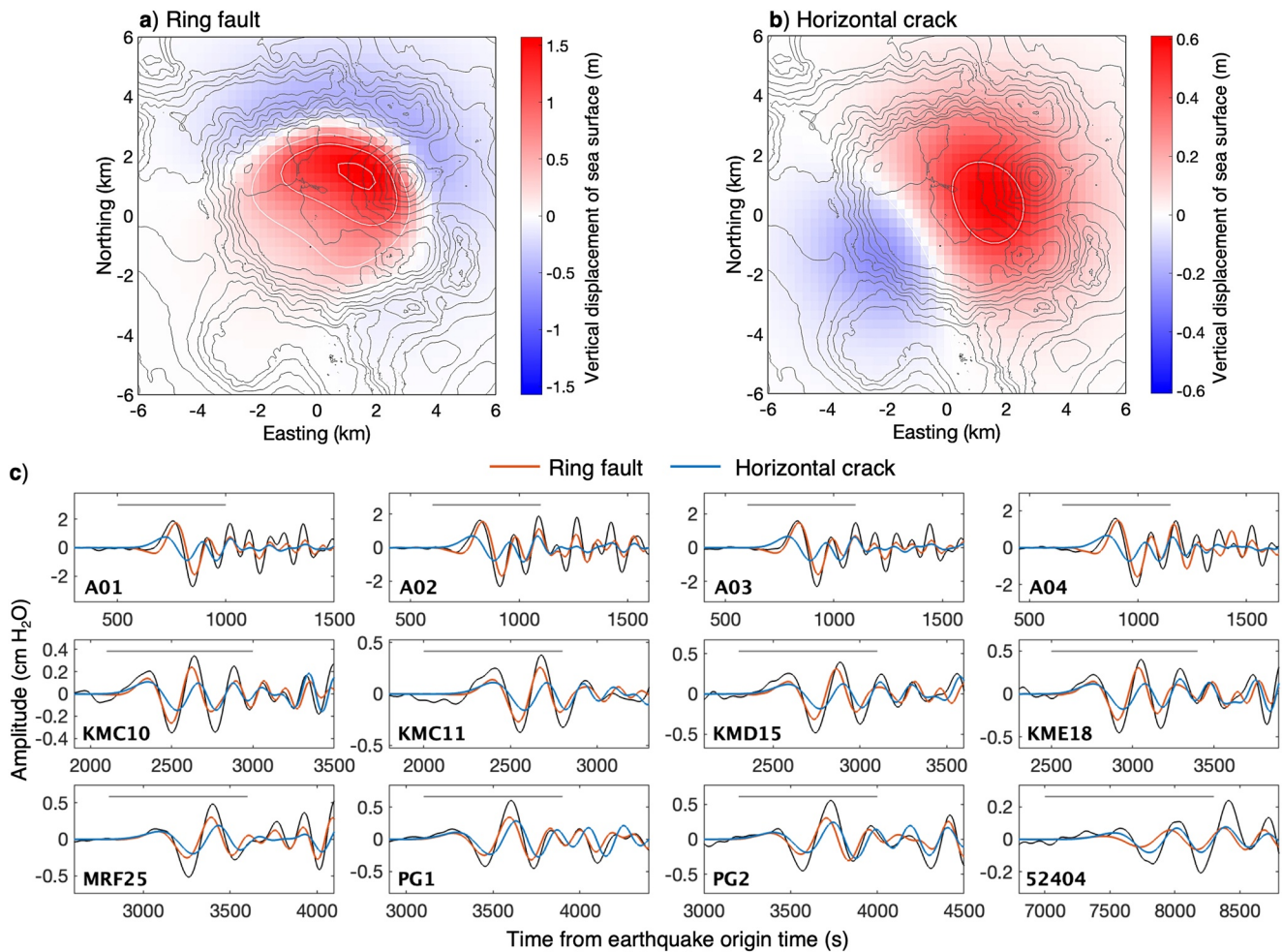**Figure 9.** Partial contributions of the ring fault and the horizontal crack of the best-fit source model (Figure 4a) to the tsunami waveforms. (a–b) Vertical sea-surface displacements caused by (a) the ring fault and (b) the horizontal crack. Red and blue colors represent uplift and subsidence, respectively, with white contour lines plotted every 0.5 m. (c) Comparison of the synthetic tsunami waveforms from the ring fault (red) and the horizontal crack (blue), with the observed (black) waveforms at representative ocean bottom pressure gauges. The gray line represents the time interval used for the inversion.

seismic excitations from the horizontal crack and the two elements ($M_{r\theta}$ and $M_{r\phi}$) of the ring fault that occur at shallow depths near the free-traction seafloor surface (pp. 180–183 of Dahlen & Tromp, 1998; Fukao et al., 2018; Sandanbata, Kanamori, et al., 2021). Thus, despite the seismic magnitude M_w 6.16 of $\boldsymbol{M}_{HC} + \boldsymbol{M}_{RF}$ (a seismic moment $M_0 = 2.16 \times 10^{18}$ Nm; Figure 8a), only the limited part of the ring-faulting $\boldsymbol{M}_{RF}$, excluding the two elements, that corresponds to M_w 5.71 ($M_0 = 0.46 \times 10^{18}$ Nm; equivalent to 22% of the total seismic moment; Figure 10c), contributes the long-period seismic radiation of the fault-crack composite source model. We note that the four moment tensor elements of the ring fault contributing to the seismic waves constitute a vertical-T CLVD-type moment tensor (Figure 10c), which agrees with the solution reported in the GCMT catalog (Ekström et al., 2012) (Figure 1b).

6. Discussion

6.1. Submarine Trapdoor Faulting at Sumisu Caldera

We have shown that the fault-crack composite source model (Figure 4a) explains quantitatively both the tsunami and long-period seismic data from the 2015 earthquake at Sumisu caldera. This source model strongly suggests the *trapdoor faulting* mechanism of the earthquake at the submarine caldera (Figure 11), like that found at the subaerial Sierra Negra caldera. As introduced briefly in Section 4.1, trapdoor faulting events have been observed geodetically several times at Sierra Negra caldera (e.g., Amelung et al., 2000; Chadwick et al., 2006;
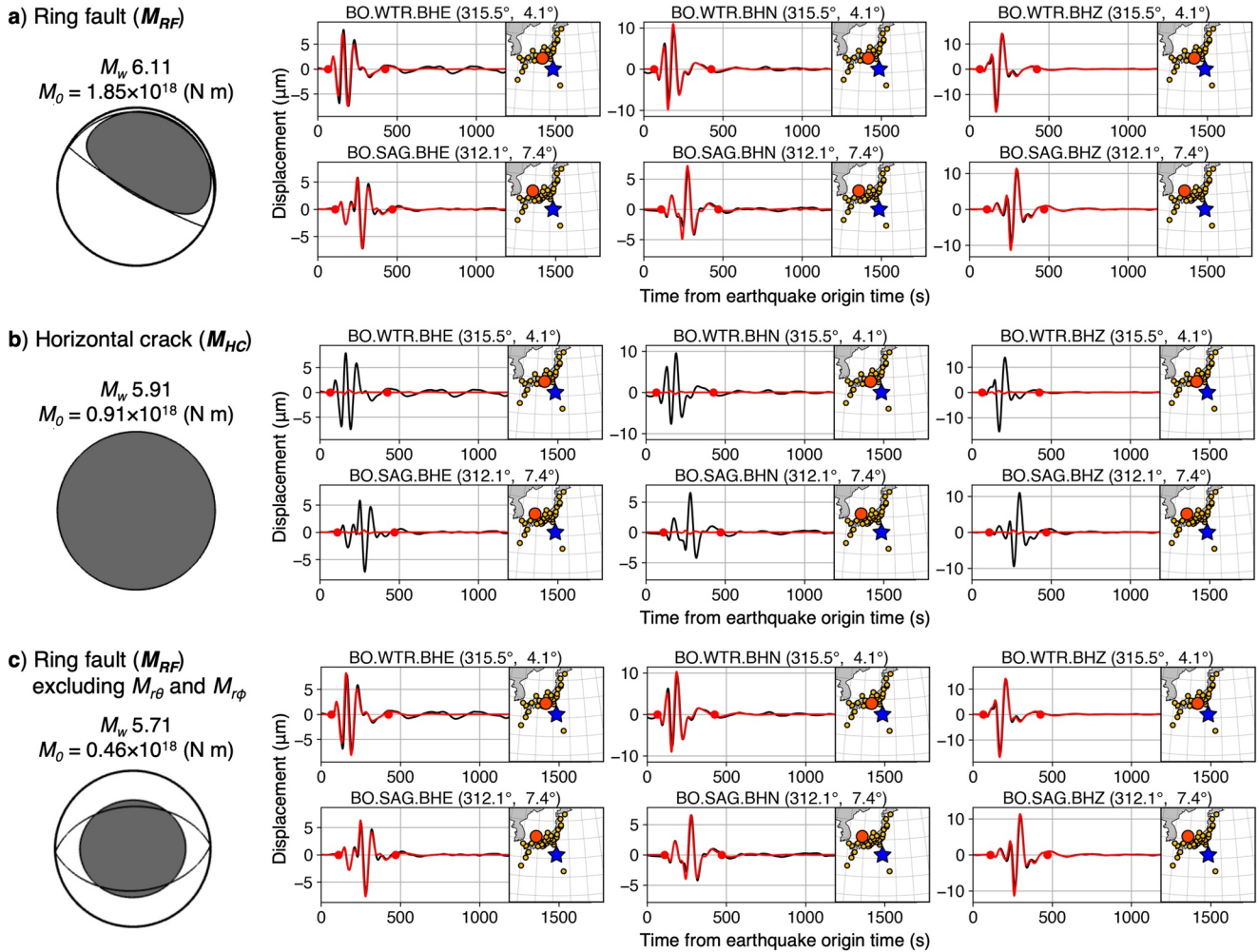
Figure 10. Contributions of the best-fit source model (Figure 4a) to the long-period seismic waves. Synthetic seismograms (red curves) from the moment tensors of (a) the ring fault M_{RF}, (b) and the horizontal crack M_{HC}, and (c) the ring fault, but excluding the two elements $M_{r\theta}$ and $M_{r\phi}$ (i.e., M_{rr}, $M_{\theta\theta}$, $M_{\phi\phi}$, and $M_{\theta\phi}$ of M_{RF}). Note that the synthetic seismic waveforms from the horizontal crack (b) are much smaller than those from the ring fault (a), and that the waveforms from the ring fault do not change although $M_{r\theta}$ and $M_{r\phi}$ are removed (compare the synthetic waveforms in a and c).

Jónsson, 2009). Based on geodetic data, many previous studies showed that the trapdoor faulting takes place in the interaction between sudden rupture of the intra-caldera ring fault and deformation of its underlying sill-like magma reservoir, and suggested that it is driven by high magma pressure within the reservoir (Amelung et al., 2000; Gregg et al., 2018; Jónsson, 2009; Yun, 2007). Recently, Zheng et al. (2022) numerically solved the mechanical interaction between the ring fault and the crack-like reservoir with magma pressure change effect, and proposed a trapdoor faulting model by fitting the geodetical data for the 2005 event of Sierra Negra caldera. Their mechanical model predicted that the trapdoor faulting caused large reverse slip of a part of an inward-dipping ring fault and asymmetric deformation of the crack-like reservoir (see Figure 2b in Zheng et al., 2022). Although our kinematic source model of the earthquake at Sumisu caldera does not consider the mechanical interaction or magma pressure change effect, the fault-crack motion patterns shown in our model (Figure 4a) are similar to those of the trapdoor faulting predicted by the mechanical model of Zheng et al. (2022).

In addition to the model similarities, trapdoor faulting events at Sierra Negra caldera share many similar features with the Sumisu caldera earthquake. First, trapdoor faulting events at Sierra Negra occurred with vertical-T CLVD earthquakes of $M_w \sim 5$ (Sandanbata, Kanamori, et al., 2021; Shuler, Ekström, & Nettles, 2013) and caused meter-scale asymmetrical caldera floor uplifts (Amelung et al., 2000; Chadwick et al., 2006; Jónsson, 2009). Second, the deformation during a trapdoor faulting in 2005 at Sierra Negra recorded by a Global Positioning System sensor near the southern intra-caldera fault occurred within 10 s (Chadwick et al., 2006; Jónsson, 2009),
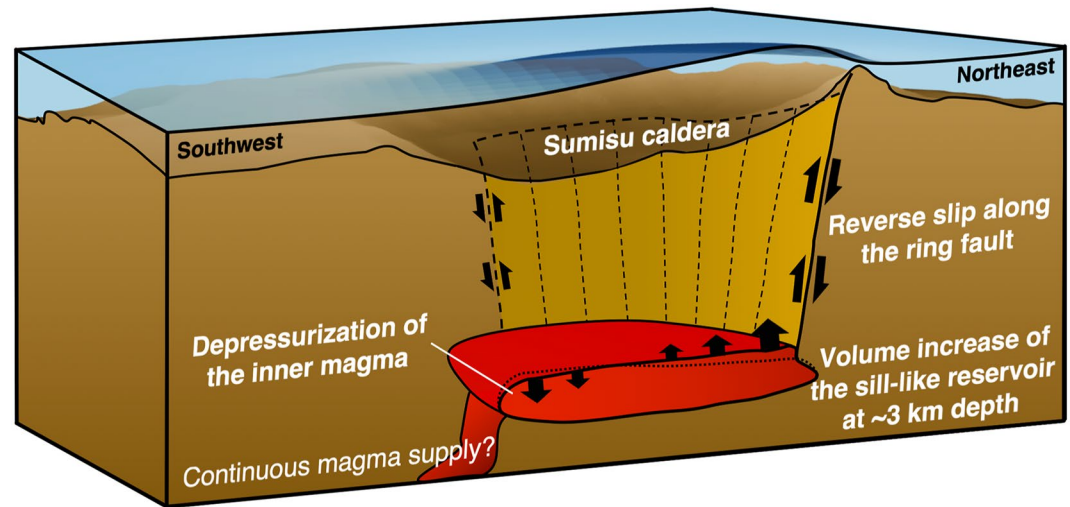
Figure 11. Schematic illustration of submarine trapdoor faulting mechanism at Sumisu caldera (not to scale). Reverse slip occurs along the ring fault, the sill-like reservoir opens vertically on the northeastern side of the caldera and consequent depressurization of the inner magma causes the downward motion of the upper wall of the southwestern part of the magma reservoir.

which is comparable to the rupture duration (10 s: the half duration of 5 s) estimated for the earthquakes at Sumisu caldera by our moment tensor analysis (Text S1 and Table S3 in Supporting Information S1). Third, during the 2005 trapdoor faulting at Sierra Negra, the northern caldera floor, opposite from the southern fault with the largest slip, subsided by a few centimeters, which was attributed to the pressure drop of the inner magma reservoir (Jónsson, 2009; Zheng et al., 2022). This feature can be expected similarly from our model with closure of the crack in the southwestern part of Sumisu caldera.

Therefore, similarly to interpretations for trapdoor faulting at Sierra Negra caldera in previous studies (e.g., Amelung et al., 2000; Jónsson, 2009; Zheng et al., 2022), we suggest that submarine trapdoor faulting at Sumisu caldera, driven by overpressure of magma accumulating in the horizontal crack, or a sill-like reservoir, caused the 2015 earthquake and tsunami (Figure 11). We speculate that continuous magma supply into the crack gradually increases the shear stress on the pre-existing ring fault system in the interseismic process, until it reaches a critical value for initiation of brittle rupture of the ring fault. Once the trapdoor faulting process initiates with the ring-faulting, the top surface of the horizontal crack moves vertically upward. The consequent increase in the reservoir volume depressurizes the inner magma, possibly causing the closure of the southwestern part of the crack, as shown by Zheng et al. (2022). Note that Zheng et al. (2022) suggested that the reservoir filled with compressible magma increases its inner volume during the trapdoor faulting. Hence, our model containing a net volume increase of $1.26 \times 10^7 \, \text{m}^3$ implies that the magma beneath the caldera is compressible. Due to the volume increase and depressurization of the inner magma, the trapdoor faulting may not lead to an immediate submarine eruption at the caldera (Amelung et al., 2000). Our finding of submarine trapdoor faulting, following the previous observations at the subaerial Sierra Negra caldera, indicates that this volcanic phenomenon might be more common at calderas than previously thought.

6.2. Efficient Tsunami Generation Mechanism

Trapdoor faulting produces an unusually large fault slip as compared with ordinary tectonic earthquakes and can generate a large tsunami when it occurs under water, despite its moderate earthquake magnitude. For the 2015 earthquake (M_w 5.7 in the GCMT catalog), our best-fit source model has a maximum slip of 6.8 m along the ring fault (Figure 4a). In contrast, the empirical scaling law (Wells & Coppersmith, 1994) predicts that tectonic earthquakes with the same moment magnitude have a maximum slip of only 0.17 m. The subaerial trapdoor faulting in 2005 at Sierra Negra caldera also caused a large slip of ~2 m along the intra-caldera fault, despite its small seismic body-wave magnitude of 4.6 (Jónsson, 2009; Zheng et al., 2022). These disproportionately large slips might be possible because the fault system connected to the reservoir can effectively cause slip. Additionally,

atypical source properties of trapdoor faulting such as the shallow source depth, the localized stress increase due to magma overpressure, and/or the fault–magma interaction during rupture, possibly contribute to large slips.

Submarine trapdoor faulting is efficient in generating tsunamis, even for the relatively low seismic magnitude of the earthquakes, due to its shallow and complex source structure. First, trapdoor faulting occurring above a shallow magma reservoir at a depth of <3 km more efficiently deforms the seafloor than tectonic earthquakes that typically occur at a depth of >10 km (Ward, 1982). Second, the combination of reverse slip along the ring fault and vertical motion of the horizontal crack localizes the coseismic uplift on a small area within the circular ring fault (Figure 6a and 9a–9b). As such, trapdoor faulting can generate larger tsunamis than ordinary seismic faults of an equivalent fault size. However, at such shallow depths, the vertical motion of the horizontal crack and the two moment tensor elements, $M_{r\theta}$ and $M_{r\phi}$, of the ring fault are inefficient in radiating long-period seismic waves (Fukao et al., 2018; Sandanbata, Kanamori, et al., 2021), as shown earlier in Section 5. Additionally, the curved geometry of the ring fault also reduces long-period seismic amplitudes by the geometrical cancellation of the double-couple components (Ekström, 1994; Sandanbata, Kanamori, et al., 2021; Shuler, Ekström, & Nettles, 2013).

6.3. Quasi-Regular Recurrence of Submarine Trapdoor Faulting

We suggest that continuous magma supply below Sumisu caldera causes submarine trapdoor faulting almost every decade. By additional moment tensor analysis using long-period seismic data (Text S3 in Supporting Information S1), we estimate the *resolvable moment tensor* M_{res} for the four earthquakes, which was studied in Sandanbata, Kanamori, et al. (2021) to constrain the ring fault geometry. The resolvable moment tensors characterized by the null-axis direction and the ratio of the vertical-CLVD component (k_{CLVD}), which was introduced in Sandanbata, Kanamori et al. (2021) and is explained in Text S1 in Supporting Information S1, are similar for the 1996, 2006, and 2015 earthquakes (Figures 12a–12c). These similarities indicate that, at the times of the earthquakes, trapdoor faulting occurred along almost the same ring fault segment of the source model for the 2015 earthquake (Figure 4a). This interpretation is supported by their similar tsunami waveforms recorded at tide gauges (Figures 1d–1e and Figure S1 in Supporting Information S1). The overall recurrence interval of ~10 years may correspond to the time required to accumulate enough magma overpressure within the reservoir to rupture the ring fault (Cabaniss et al., 2020; Gregg et al., 2018). On the other hand, the resolvable moment tensor for the 2018 earthquake, which occurred only three years after the 2015 earthquake, contains a more dominant double-couple component (i.e., smaller k_{CLVD}) and has a smaller moment magnitude M_w (Figure 12d), suggesting that the trapdoor faulting in 2018 caused a rupture along a ring fault segment with a shorter arc length than those for the other events. This may explain the smaller tsunami associated with the 2018 earthquake (Figures 1d–1e and Figure S1 in Supporting Information S1). Some complexities linked to source geometries, frictional properties along the ring fault, or magma supply rate may cause variations in the size, the ring-fault length, and the recurrence interval of trapdoor faulting. For seismic waveform comparison, we show the results of moment tensor analyses for the four events in Figures S16–S19 in Supporting Information S1.

The topography of Sumisu caldera also reflects the longer-term recurrence of trapdoor faulting. Our source model predicts that the submarine trapdoor faulting in 2015 uplifted the northeastern part of the caldera floor but caused little deformation in its southwestern part (Figure 12e). Along a SW–NE profile across the caldera (A–B in Figure 12e), coseismic vertical displacement with an offset of about 4 m correlates with the caldera floor topography, which slopes upward from the SW to NE with an altitude offset of ~150 m (Figure 12f). A similar correlation was found at Sierra Negra caldera (Amelung et al., 2000), where trapdoor faulting has occurred repeatedly due to continuous magma input. This suggests that magma supply has been continuous at Sumisu caldera, thereby causing submarine trapdoor faulting repeatedly and forming the slope of the caldera floor. Since an explosive submarine eruption in 1916 (Japan Meteorological Agency, 2013), no clear evidence of eruptions has been found at Sumisu caldera and the relationship between trapdoor faulting and eruptions is still unclear.

6.4. Mechanisms of Volcanic Tsunami Generation

Various mechanisms have been proposed to generate volcanic tsunamis: submarine explosions, pyroclastic flows, flank failures, caldera collapses, volcanic earthquakes accompanying eruptions, and interactions of ocean waves with atmospheric waves from volcanic explosions (Paris, 2015; Paris et al., 2014). The submarine trapdoor
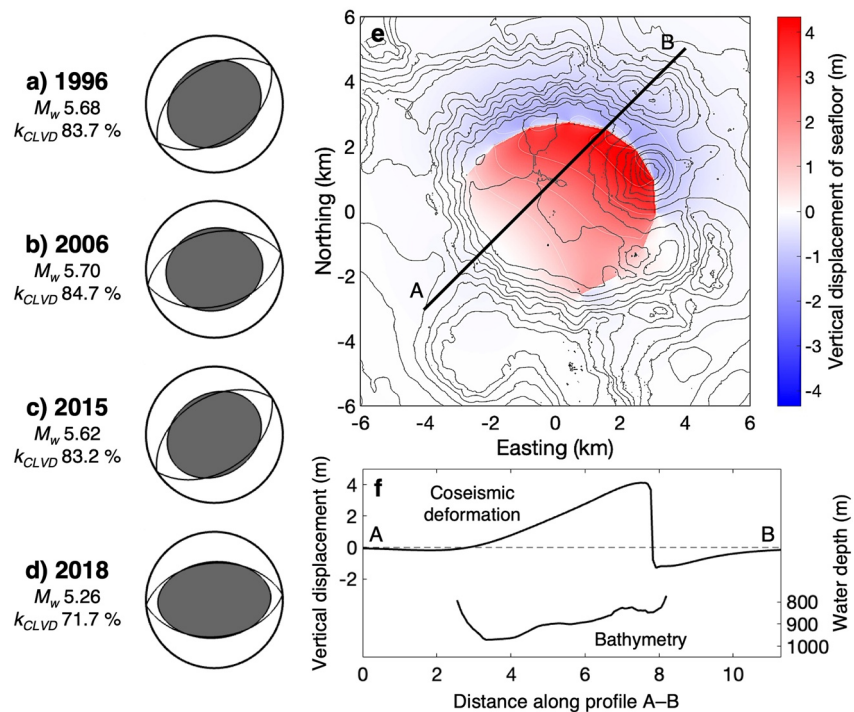
Figure 12. Recurrence of trapdoor faulting at Sumisu caldera. (a–d) Resolvable moment tensors M_{res} for the earthquakes in (a) 1996, (b) 2006, (c) 2015, and (d) 2018 estimated by our moment tensor analysis. The orientation of the best double-couple solution is shown by thin curves. M_w and k_{CLVD} indicate the moment magnitude of M_{res} and the dominancy of the vertical-compensated-linear-vector-dipole component in M_{res}, respectively. (e) Vertical seafloor displacement computed with the best-fit source model for the 2015 earthquake (Figure 4a). (f) Profiles of the vertical seafloor displacement and the topography along A–B shown in (e).

faulting mechanism identified in this study may be categorized as a volcanic earthquake mechanism, but is characterized by large-amplitude tsunamis without significant seismic radiation and by quasi-regular recurrence. This mechanism may also explain unusual tsunamis with similar characteristics generated near volcanic islands in the Kermadec arc, north of New Zealand (Gusman et al., 2020). These volcanic tsunamis due to submarine trapdoor faulting suggest that continuous monitoring of submarine calderas is necessary to reliably assess tsunami hazards.

7. Conclusions

By using remotely observed tsunami and long-period seismic data from the 2015 earthquake at Sumisu caldera, we constructed a fault-crack composite source model of submarine trapdoor faulting, which can quantitatively explain both datasets. The combined waveform analyses also allow us to constrain the magma reservoir depth and the ring fault geometry. Based on the model, we show that the atypical source properties, or large slip on a shallow and complex structure, contributed to meter-scale tsunami generation despite the moderate seismic magnitude. The sub-decadal recurrence of trapdoor faulting with similar tsunamis and seismic characters suggests that continuous magma supply into the submarine caldera has been taking place. Further investigations of the submarine caldera using in situ geophysical instruments, such as hydrophones, seismometers, pressure sensors, and ship-borne surveys will be useful for understanding the volcanism, including the magma accumulation process. This may lead to improved predictions of future submarine trapdoor faulting and/or eruptions.

Data Availability Statement

The earthquake data are from the Global CMT catalog (Ekström et al., 2012; https://www.globalcmt.org/). Tide gauge data are available on request from the Japan Meteorological Agency (https://www.jma.go.jp/jma/indexe.html) and Hydrographic and Oceanographic Department, Japan Coast Guard (https://www1.kaiho.mlit.go.jp/TIDE/gauge/index_eng.php) upon requests. Bathymetric data of M7000 Digital Bathymetric Chart and JTOPO30

are available from the Japan Hydrographic Association (https://www.jha.or.jp/shop/index.php?main_page=index) and GEBCO_2014 Grid is available from GEBCO Compilation Group (Weatherall et al., 2015; https://www.gebco.net/data_and_products/gridded_bathymetry_data/gebco_30_second_grid/). Ocean bottom pressure data of the array off Aogashima Island (Fukao et al., 2019) and the Deep Sea Floor Observatory off Muroto Cape (Momma et al., 1997) are available from the Japan Agency for Marine-Earth Science and Technology (http://p21.jamstec.go.jp/top/; under construction at the time of publication), DONET data are available from National Research Institute for Earth Science and Disaster Resilience (National Research Institute for Earth Science and Disaster Resilience, 2019a; https://www.seafloor.bosai.go.jp/), and DART data is available from National Oceanic and Atmospheric Administration (National Oceanic and Atmospheric Administration. 2005; https://nctr.pmel.noaa.gov/Dart/). F-net seismic data of F-net are available from the NIED (National Research Institute for Earth Science and Disaster Resilience, 2019b; https://www.fnet.bosai.go.jp/top.php?LANG=en), and Global Seismograph Network data are available through the IRIS Wilber 3 system (https://ds.iris.edu/wilber3/) or IRIS Web Services (https://service.iris.edu/), including the IU seismic network (GSN; Albuquerque, 1988). The source models presented in this paper are detailed in Data Set S1, which is available from Zenodo (https://zenodo.org/record/6983982).

References

Aki, K., & Richards, P. G. (1980). *Quantitative seismology: Theory and methods* (Vol. 842). Freeman.

Albuquerque Seismological Laboratory (ASL)/USGS. (1988). Global Seismograph network (GSN–IRIS/USGS) [Data set]. International Federation of Digital Seismograph Networks. Retrieved from https://pubs.geoscienceworld.org/ssa/srl/article-abstract/91/4/2425/586807/Installation-and-Performance-of-the-Albuquerque

Amelung, F., Jónsson, S., Zebker, H., & Segall, P. (2000). Widespread uplift and "trapdoor" faulting on Galápagos volcanoes observed with radar interferometry. *Nature*, *407*(6807), 993–996. https://doi.org/10.1038/35039604

Baba, T., Takahashi, N., Kaneda, Y., Ando, K., Matsuoka, D., & Kato, T. (2015). Parallel implementation of dispersive tsunami wave modeling with a nesting algorithm for the 2011 Tohoku tsunami. *Pure and Applied Geophysics*, *172*(12), 3455–3472. https://doi.org/10.1007/s00024-015-1049-2

Bathke, H., Nikkhoo, M., Holohan, E. P., & Walter, T. R. (2015). Insights into the 3D architecture of an active caldera ring-fault at Tendürek volcano through modeling of geodetic data. *Earth and Planetary Science Letters*, *422*, 157–168. https://doi.org/10.1016/j.epsl.2015.03.041

Cabaniss, H. E., Gregg, P. M., Nooner, S. L., & Chadwick, W. W., Jr. (2020). Triggering of eruptions at axial Seamount, Juan de Fuca Ridge. *Scientific Reports*, *10*(1), 10219. https://doi.org/10.1038/s41598-020-67043-0

Chadwick, W. W., Geist, D. J., Jónsson, S., Poland, M., Johnson, D. J., & Meertens, C. M. (2006). A volcano bursting at the seams: Inflation, faulting, and eruption at Sierra Negra volcano, Galápagos. *Geology*, *34*(12), 1025–1028. https://doi.org/10.1130/G22826A.1

Chikasada, N. Y. (2019). Short-wavelength tsunami observation using deep ocean bottom pressure gauges. In *The 29th international ocean and polar engineering conference*. International Society of Offshore and Polar Engineers. Retrieved from https://onepetro.org/conference-paper/ISOPE-I-19-707

Cole, J. W., Milner, D. M., & Spinks, K. D. (2005). Calderas and caldera structures: A review. *Earth-Science Reviews*, *69*(1), 1–26. https://doi.org/10.1016/j.earscirev.2004.06.004

Contreras-Arratia, R., & Neuberg, J. W. (2019). Complex seismic sources in volcanic environments: Radiation modelling and moment tensor inversions. *Journal of Volcanology and Geothermal Research*, *381*, 262–272. https://doi.org/10.1016/j.jvolgeores.2019.06.005

Dahlen, F. A., & Tromp, J. (1998). *Theoretical global seismology*. Princeton University Press.

Duputel, Z., Rivera, L., Kanamori, H., & Hayes, G. (2012). W phase source inversion for moderate to large earthquakes (1990–2010). *Geophysical Journal International*, *189*(2), 1125–1147. https://doi.org/10.1111/j.1365-246X.2012.05419.x

Ekström, G. (1994). Anomalous earthquakes on volcano ring-fault structures. *Earth and Planetary Science Letters*, *128*(3–4), 707–712. https://doi.org/10.1016/0012-821x(94)90184-8

Ekström, G., Nettles, M., & Dziewoński, A. M. (2012). The global CMT project 2004–2010: Centroid-moment tensors for 13,017 earthquakes. *Physics of the Earth and Planetary Interiors*, *200*, 1–9. https://doi.org/10.1016/j.pepi.2012.04.002

Fukao, Y., Miyama, T., Tono, Y., Sugioka, H., Ito, A., Shiobara, H., et al. (2019). Detection of ocean internal tide source oscillations on the slope of Aogashima Island, Japan. *Journal of Geophysical Research—C: Oceans*, *124*(7), 4918–4933. https://doi.org/10.1029/2019jc014997

Fukao, Y., Sandanbata, O., Sugioka, H., Ito, A., Shiobara, H., Watada, S., & Satake, K. (2018). Mechanism of the 2015 volcanic tsunami earthquake near Torishima, Japan. *Science Advances*, *4*(4), eaao0219. https://doi.org/10.1126/sciadv.aao0219

Galetto, F., Bagnardi, M., Acocella, V., & Hooper, A. (2019). Noneruptive unrest at the caldera of Alcedo volcano (Galápagos Islands) revealed by InSAR data and geodetic modeling. *Journal of Geophysical Research: Solid Earth*, *124*(4), 3365–3381. https://doi.org/10.1029/2018jb017103

Gregg, P. M., Le Mével, H., Zhan, Y., Dufek, J., Geist, D., & Chadwick, W. W., Jr. (2018). Stress triggering of the 2005 eruption of Sierra Negra volcano, Galápagos. *Geophysical Research Letters*, *45*(24), 13288–13297. https://doi.org/10.1029/2018gl080393

Grilli, S. T., Tappin, D. R., Carey, S., Watt, S. F. L., Ward, S. N., Grilli, A. R., et al. (2019). Modelling of the tsunami from the December 22, 2018 lateral collapse of anak Krakatau volcano in the Sunda Straits, Indonesia. *Scientific Reports*, *9*(1), 11946. https://doi.org/10.1038/s41598-019-48327-6

Gusman, A. R., Kaneko, Y., Power, W., & Burbidge, D. (2020). Source process for two enigmatic repeating vertical-T CLVD tsunami earthquakes in the Kermadec ridge. *Geophysical Research Letters*, *47*(16). https://doi.org/10.1029/2020gl087805

Hanks, T. C., & Kanamori, H. (1979). A moment magnitude scale. *Journal of Geophysical Research*, *84*(B5), 2348. https://doi.org/10.1029/jb084ib05p02348

Hayes, G. P., Rivera, L., & Kanamori, H. (2009). Source inversion of the W-phase: Real-time implementation and extension to low magnitudes. *Seismological Research Letters*, *80*(5), 817–822. https://doi.org/10.1785/gssrl.80.5.817

Herrmann, R. B. (2013). Computer programs in Seismology: An evolving Tool for instruction and Research. *Seismological Research Letters*, *84*(6), 1081–1088. https://doi.org/10.1785/0220110096

Ho, T.-C., Satake, K., & Watada, S. (2017). Improved phase corrections for transoceanic tsunami data in spatial and temporal source estimation: Application to the 2011 Tohoku earthquake. *Journal of Geophysical Research: Solid Earth*, *122*(12), 10155–10175. https://doi.org/10.1002/2017jb015070

Hossen, M. J., Cummins, P. R., Dettmer, J., & Baba, T. (2015). Time reverse imaging for far-field tsunami forecasting: 2011 Tohoku earthquake case study. *Geophysical Research Letters*, *42*(22), 9906–9915. https://doi.org/10.1002/2015gl065868

Hunt, J. E., Tappin, D. R., Watt, S. F. L., Susilohadi, S., Novellino, A., Ebmeier, S. K., et al. (2021). Submarine landslide megablocks show half of Anak Krakatau island failed on December 22nd, 2018. *Nature Communications*, *12*(1), 2827. https://doi.org/10.1038/s41467-021-22610-5

Japan Meteorological Agency. (2013). National catalogue of the active volcanoes in Japan. Retrieved from https://www.data.jma.go.jp/svd/vois/data/tokyo/STOCK/souran_eng/menu.htm

Jónsson, S. (2009). Stress interaction between magma accumulation and trapdoor faulting on Sierra Negra volcano, Galápagos. *Tectonophysics*, *471*(1), 36–44. https://doi.org/10.1016/j.tecto.2008.08.005

Kajiura, K. (1963). The leading wave of a tsunami. *Bulletin of the Earthquake Research Institute, University of Tokyo*, *41*(3), 535–571. Retrieved from https://ci.nii.ac.jp/naid/120000866529/

Kanamori, H. (1972). Mechanism of tsunami earthquakes. *Physics of the Earth and Planetary Interiors*, *6*(5), 346–359. https://doi.org/10.1016/0031-9201(72)90058-1

Kanamori, H. (1977). The energy release in great earthquakes. *Journal of Geophysical Research*, *82*(20), 2981–2987. https://doi.org/10.1029/jb082i020p02981

Kanamori, H., Ekström, G., Dziewonski, A., Barker, J. S., & Sipkin, S. A. (1993). Seismic radiation by magma injection: An anomalous seismic event near Tori Shima, Japan. *Journal of Geophysical Research*, *98*(B4), 6511–6522. https://doi.org/10.1029/92jb02867

Kanamori, H., & Rivera, L. (2008). Source inversion of Wphase: Speeding up seismic tsunami warning. *Geophysical Journal International*, *175*(1), 222–238. https://doi.org/10.1111/j.1365-246X.2008.03887.x

Kawakatsu, H., & Yamamoto, M. (2015). 4.15—Volcano seismology. In G. Schubert (Ed.), (Ed), *Treatise on geophysics* (2nd edn, pp. 389–419). Elsevier. https://doi.org/10.1016/B978-0-444-53802-4.00081-6

Liu, Y.-K., Ruch, J., Vasyura-Bathke, H., & Jónsson, S. (2019). Influence of ring faulting in localizing surface deformation at subsiding calderas. *Earth and Planetary Science Letters*, *526*, 115784. https://doi.org/10.1016/j.epsl.2019.115784

Momma, H., Fujiwara, N., Kawaguchi, K., Iwase, R., Suzuki, S., & Kinoshita, H. (1997). Monitoring system for submarine earthquakes and deep sea environment. *Oceans'97. MTS/IEEE Conference Proceedings*, *2*, 1453–1459. https://doi.org/10.1109/OCEANS.1997.624211

National Oceanic and Atmospheric Administration. (2005). Deep-ocean assessment and reporting of tsunamis (DART) [Data set]. National Geophysical Data Center. Retrieved from https://www.ndbc.noaa.gov/dart/milburn_1996.shtml

National Research Institute for Earth Science and Disaster Resilience. (2019a). NIED DONET [Data set]. National Research Institute for Earth Science and Disaster Resilience. https://doi.org/10.17598/NIED.0008. Retrieved from https://www.seafloor.bosai.go.jp

National Research Institute for Earth Science and Disaster Resilience. (2019b). NIED F-net [Data set]. National Research Institute for Earth Science and Disaster Resilience. https://doi.org/10.17598/NIED.0005. Retrieved from https://www.fnet.bosai.go.jp/top.php?LANG=en

Nikkhoo, M., & Walter, T. R. (2015). Triangular dislocation: An analytical, artefact-free solution. *Geophysical Journal International*, *201*(2), 1119–1141. https://doi.org/10.1093/gji/ggv035

Paris, R. (2015). Source mechanisms of volcanic tsunamis. *Philosophical Transactions. Series A, Mathematical, Physical, and Engineering Sciences*, *373*(2053), 20140380. https://doi.org/10.1098/rsta.2014.0380

Paris, R., Switzer, A. D., Belousova, M., Belousov, A., Ontowirjo, B., Whelley, P. L., & Ulvrova, M. (2014). Volcanic tsunami: A review of source mechanisms, past events and hazards in Southeast Asia (Indonesia, Philippines, Papua New Guinea). *Natural Hazards*, *70*(1), 447–470. https://doi.org/10.1007/s11069-013-0822-8

Peregrine, D. H. (1972). Equations for water waves and the approximation behind them. In R. E. Meyer (Ed.), (Ed), *Waves on beaches and resulting sediment transport* (pp. 95–121). Academic Press. https://doi.org/10.1016/B978-0-12-493250-0.50007-2

Persson, P.-O., & Strang, G. (2004). A Simple Mesh generator in MATLAB. *SIAM Review. Society for Industrial and Applied Mathematics*, *46*(2), 329–345. https://doi.org/10.1137/s0036144503429121

Roche, O., Druitt, T. H., & Merle, O. (2000). Experimental study of caldera formation. *Journal of Geophysical Research*, *105*(B1), 395–416. https://doi.org/10.1029/1999jb900298

Saito, T., & Furumura, T. (2009). Three-dimensional tsunami generation simulation due to sea-bottom deformation and its interpretation based on the linear theory. *Geophysical Journal International*, *178*(2), 877–888. https://doi.org/10.1111/j.1365-246X.2009.04206.x

Sandanbata, O., Kanamori, H., Rivera, L., Zhan, Z., Watada, S., & Satake, K. (2021). Moment tensors of ring-faulting at active volcanoes: Insights into vertical-CLVD earthquakes at the Sierra Negra caldera, Galápagos Islands. *Journal of Geophysical Research: Solid Earth*, *126*(6), e2021JB021693. https://doi.org/10.1029/2021jb021693

Sandanbata, O., Watada, S., Ho, T.-C., & Satake, K. (2021). Phase delay of short-period tsunamis in the density-stratified compressible ocean over the elastic Earth. *Geophysical Journal International*, *226*(3), 1975–1985. https://doi.org/10.1093/gji/ggab192

Satake, K. (2015). 4.19—Tsunamis. In G. Schubert (Ed.), (Ed), *Treatise on geophysics* (2nd edn, pp. 477–504). Elsevier. https://doi.org/10.1016/B978-0-444-53802-4.00086-5

Satake, K., & Kanamori, H. (1991). Abnormal tsunamis caused by the June 13, 1984, Torishima, Japan, earthquake. *Journal of Geophysical Research*, *96*(B12), 19933–19939. https://doi.org/10.1029/91jb01903

Shukuno, H., Tamura, Y., Tani, K., Chang, Q., Suzuki, T., & Fiske, R. S. (2006). Origin of silicic magmas and the compositional gap at Sumisu submarine caldera, Izu–Bonin arc, Japan. *Journal of Volcanology and Geothermal Research*, *156*(3), 187–216. https://doi.org/10.1016/j.jvolgeores.2006.03.018

Shuler, A., Ekström, G., & Nettles, M. (2013). Physical mechanisms for vertical-CLVD earthquakes at active volcanoes. *Journal of Geophysical Research: Solid Earth*, *118*(4), 1569–1586. https://doi.org/10.1002/jgrb.50131

Shuler, A., Nettles, M., & Ekström, G. (2013). Global observation of vertical-CLVD earthquakes at active volcanoes. *Journal of Geophysical Research: Solid Earth*, *118*(1), 138–164. https://doi.org/10.1029/2012jb009721

Silver, P. G., & Jordan, T. H. (1982). Optimal estimation of scalar seismic moment. *Geophysical Journal International*, *70*(3), 755–787. https://doi.org/10.1111/j.1365-246X.1982.tb05982.x

Tani, K., Fiske, R. S., Tamura, Y., Kido, Y., Naka, J., Shukuno, H., & Takeuchi, R. (2008). Sumisu volcano, Izu–Bonin Arc, Japan: Site of a silicic caldera-forming eruption from a small open-ocean island. *Bulletin of Volcanology*, *70*(5), 547–562. https://doi.org/10.1007/s00445-007-0153-2

Tappin, D. R., Matsumoto, T., Watts, P., Satake, K., McMurtry, G. M., Matsuyama, M., et al. (1999). Sediment slump likely caused 1998 Papua New Guinea tsunami. *Eos*, *80*(30), 329. https://doi.org/10.1029/99eo00241

Walter, T. R., Haghshenas Haghighi, M., Schneider, F. M., Coppola, D., Motagh, M., Saul, J., et al. (2019). Complex hazard cascade culminating in the Anak Krakatau sector collapse. *Nature Communications*, *10*(1), 4339. https://doi.org/10.1038/s41467-019-12284-5

Ward, S. N. (1982). On tsunami nucleation II. An instantaneous modulated line source. *Physics of the Earth and Planetary Interiors*, *27*(4), 273–285. https://doi.org/10.1016/0031-9201(82)90057-7

Ward, S. N. (2001). Landslide tsunami. *Journal of Geophysical Research*, *106*(B6), 11201–11215. https://doi.org/10.1029/2000jb900450

Weatherall, P., Marks, K. M., Jakobsson, M., Schmitt, T., Tani, S., Arndt, J. E., et al. (2015). A new digital bathymetric model of the world's oceans. *Earth in Space*, *2*(8), 331–345. https://doi.org/10.1002/2015EA000107

Wells, D. L., & Coppersmith, K. J. (1994). New empirical Relationships among magnitude, Rupture length, Rupture Width, Rupture area, and surface displacement. *Bulletin of the Seismological Society of America*, *84*(4), 974–1002. https://doi.org/10.1785/BSSA0840040974

Yun, S.-H. (2007). *A mechanical model of the large-deformation 2005 Sierra Negra volcanic eruption derived from InSAR measurements, (Ph.D. Desertation)*. Stanford University. Retrieved from https://web.stanford.edu/group/radar/people/Yun_thesis_small.pdf

Zheng, Y., Blackstone, L., & Segall, P. (2022). Constraints on absolute magma chamber volume from geodetic measurements of trapdoor faulting at Sierra Negra volcano, Galapagos. *Geophysical Research Letters*, *49*(5). https://doi.org/10.1029/2021gl095683

References From the Supporting Information

Kodaira, S., Sato, T., Takahashi, N., Ito, A., Tamura, Y., Tatsumi, Y., & Kaneda, Y. (2007). Seismological evidence for variable growth of crust along the Izu intraoceanic arc. *Journal of Geophysical Research*, *112*(B5), B05104. https://doi.org/10.1029/2006jb004593